

# Materials Advances

Accepted Manuscript

This article can be cited before page numbers have been issued, to do this please use: S. Ramar, P. Sathish Kumar, B. K. Raja, M. Govindaraj and A. S. J, *Mater. Adv.*, 2026, DOI: 10.1039/D6MA00227G.



This is an Accepted Manuscript, which has been through the Royal Society of Chemistry peer review process and has been accepted for publication.

Accepted Manuscripts are published online shortly after acceptance, before technical editing, formatting and proof reading. Using this free service, authors can make their results available to the community, in citable form, before we publish the edited article. We will replace this Accepted Manuscript with the edited and formatted Advance Article as soon as it is available.

You can find more information about Accepted Manuscripts in the [Information for Authors](#).

Please note that technical editing may introduce minor changes to the text and/or graphics, which may alter content. The journal's standard [Terms & Conditions](#) and the [Ethical guidelines](#) still apply. In no event shall the Royal Society of Chemistry be held responsible for any errors or omissions in this Accepted Manuscript or any consequences arising from the use of any information it contains.

1 **Enhanced Faradaic Pseudo-capacitance in reduced  $\pi$ -conjugated carbon**  
2 **network anchored with Strontium Tungstate Nano-Hybrids for High-**  
3 **Energy Supercapacitors**

4 Sabarikaruthapandi Ramar<sup>a</sup>, Ponnaiah Sathish Kumar<sup>b</sup>, Bharathi Kannan Raja<sup>a</sup>,  
5 Muthukumar Govindaraj<sup>a,c</sup>, and Arockia Selvi J<sup>a\*</sup>

6  
7  
8 <sup>a</sup>Department of Chemistry, SRM Institute of Science and Technology, Kattankulathur  
9 603203, Tamil Nadu, India.

10 <sup>b</sup>Department of Chemical Engineering, Pohang University of Science and Technology  
11 (POSTECH), Pohang 37673, Republic of Korea.

12 <sup>c</sup>Institute of Industrial Science, The University of Tokyo, 4-6-1 Komaba, Meguro-Ku,  
13 Tokyo 153–8505, Japan.

14  
15  
16  
17  
18  
19  
20  
21  
22  
23  
24  
25  
26  
27  
28  
29  
30  
31  
32 **Corresponding author**

33 E-mail: [arockiaj@srmist.edu.in](mailto:arockiaj@srmist.edu.in) (Prof. Dr. Arockia Selvi J)



## 1 Abstract

2 The development of high-performance electrode materials is essential for next-generation  
3 supercapacitor (SC) technologies. In this work, SrWO<sub>4</sub>/rGO hybrid nanostructures were  
4 synthesized to enhance electrochemical performance through the synergistic effect of  
5 conductive SrWO<sub>4</sub> and high-surface-area reduced graphene oxide (rGO). This hybrid electrode  
6 material displays excellent electrochemical execution, delivering an excellent specific  
7 capacitance of 727 F g<sup>-1</sup> at 1 A g<sup>-1</sup> and asserted 95% of its capacitance over 5000 cycles,  
8 indicating extended stability. The asserted symmetric two-electrode cell  
9 (SrWO<sub>4</sub>/rGO@NF//SrWO<sub>4</sub>/rGO@NF) operates within a 1.6 V potential window in 1 M KOH  
10 electrolyte and shows excellent rate capability. Electrochemical impedance spectroscopy of a  
11 symmetric cell reveals low charge-transfer resistance and efficient ion diffusion. The Ragone  
12 plot highlights an impressive energy density of 26.13 Wh kg<sup>-1</sup> at a power density of  
13 2159.5 W kg<sup>-1</sup> for the assembled symmetric cell. This exceptional performance is attributed  
14 to the synergistic effect of conductive SrWO<sub>4</sub> and the higher surface area, stemming from its  
15 resorted  $\pi$ -conjugated rGO structure, enabling efficient charge transport and abundant  
16 electroactive sites. These results highlight a promising strategy for developing advanced  
17 electrode materials for high-performance energy storage systems.

18

19

20

21

22

23

24

25 **Keywords:** Ternary metal oxides; SrWO<sub>4</sub>/rGO; Symmetric devices; Specific capacitance;  
26 Energy storage devices.

27

28



## 1. Introduction

The urgent need to address fossil fuel scarcity, environmental degradation, and increasing energy consumption has urged innovation in alternative energy storage and conversion systems. The increasing demand for sustainable and efficient energy storage solutions has spurred extensive research on supercapacitors (SCs), which play an essential role in advancing electronics, electric vehicles, and renewable energy technologies.<sup>1-3</sup> high-power density, rapid charge/discharge rates, and excellent cyclic stability, SCs stand as effective alternatives to conventional batteries.<sup>4-6</sup> To meet growing energy demands, it's essential to develop durable, high-performance systems that integrate technologies.<sup>7-9</sup> In this context, SCs are broadly classified into three categories: electrochemical double-layer capacitors (EDLCs), which store charge via non-Faradaic charge separation; pseudocapacitive materials, which rely on fast and reversible redox reactions; and hybrid capacitors, which combine both pseudocapacitive and non-Faradaic double-layer (NFDL) charge storage mechanisms. Among these, hybrid capacitors have emerged as a particularly promising approach for enhancing SC performance due to their ability to deliver high energy density, stable operating voltage, high specific capacitance, and excellent cycling stability. Consequently, extensive efforts have been devoted to exploring SC electrodes, including ternary metal oxides (TMOs) and binary metal oxides (BMOs) that contain at least one electrochemically active metal cation and an oxygen anion. Both pure and bimetallic oxide materials can synergistically enhance capacitive performance by offering improved stability, wider potential windows, higher conductivity, greater reversible capacity, and more active sites.<sup>10-18</sup> Among BMOs, inorganic structured metal oxides such as Scheelite-type metal tungstates with the formula  $MWO_4$  (where M = Ni, Mg, Zn, Sr, Cu, Co, Ba, Ca, Mn, etc.) are being investigated for various electrochemical applications, including energy storage.<sup>19-21</sup> Among others, strontium tungstate ( $SrWO_4$ ) has gained particular attention, owing to its high conductivity, ordered crystal structure, and abundant oxygen vacancies.<sup>22-24</sup> This performance is attributed to its crystal structure, in which  $Sr^{2+}$  occupies octahedral sites, and  $W^{6+}$  is coordinated within tetrahedral oxygen frameworks, which promote structural defects and generate numerous active sites.<sup>25, 26</sup> Similarly, carbon-based materials such as graphitic carbon nitride ( $g-C_3N_4$ ), activated carbon, and carbon nanotubes (CNTs) have emerged as promising candidates for various electrochemical applications, including electrochemical sensors and SC electrodes, owing to their large surface areas and excellent electrical conductivity. Despite these advantages, designing novel or modified electrode materials with improved specific capacitance remains a key challenge for researchers. Though



1 SrWO<sub>4</sub> is electrochemically active, it has a lower surface area due to its dense scheelite crystal  
2 structure. An effective electrocatalyst for SC requires both electrical conductivity and a high  
3 surface area to achieve higher capacitance. Hence, in this work, we aim to anchor  
4 electrochemically active and conductive SrWO<sub>4</sub> with a resorted  $\pi$ -conjugated structure of  
5 graphene oxide post reduction to fabricate SrWO<sub>4</sub>/rGO hybrid nanostructure that  
6 synergistically combines the high electrical conductivity of SrWO<sub>4</sub> and redox-active  
7 characteristics with the high surface area of rGO.

8 Reduced graphene oxide (rGO) is widely recognized as an excellent electrode material due  
9 to its restored  $\pi$ -conjugated structure, semiconducting nature, sp<sup>2</sup>-hybridised carbon network,  
10 and residual functional groups with lone-pair electrons, which collectively facilitate effective  
11 interactions with various nanomaterials.<sup>27, 28</sup> The sp<sup>2</sup>-hybridised carbon in rGO links aromatic  
12 carbon domains, thereby further enhancing electrochemical performance.<sup>29, 30</sup> sheets tend to  
13 restack face-to-face due to strong  $\pi$ - $\pi$  interactions, which significantly diminishes their  
14 electrochemical performance.<sup>31</sup> Therefore, incorporating SrWO<sub>4</sub> as a pseudocapacitive  
15 component prevents graphene aggregation and improves specific capacitance.<sup>32, 33</sup> There were  
16 reports that present SrWO<sub>4</sub>-based electrode materials for SC applications, for instance, S.  
17 Rajakumar *et.al.* fabricated SrWO<sub>4</sub>/PPy electrode and achieved a high specific capacitance  
18 (747 Fg<sup>-1</sup> at 5 mVs<sup>-1</sup>) with good stability (5000 cycles).<sup>11</sup> In addition, E. Umar *et al.*  
19 designed well-established SrWO<sub>4</sub>/g-C<sub>3</sub>N<sub>4</sub>, which shows improved electrochemical  
20 performance for both HER and a hybrid energy storage device.<sup>34</sup> Furthermore, B. Muthukutty  
21 *et.al.* prepared SrWO<sub>4</sub> anchored in a boron nitride matrix, which exhibited improved  
22 electrochemical performance for electrochemical sensing of ornidazole.<sup>19</sup> These reports  
23 demonstrate SrWO<sub>4</sub> hybrid structures capable of achieving high electrochemical performance  
24 through morphological tuning, interface engineering, surface modifications, and the fabrication  
25 of hybrid nanocomposites. In a broader context, metal tungstates (WO<sub>4</sub><sup>2-</sup>) have attracted  
26 significant attention due to their excellent electrochemical, magnetic, and catalytic properties,  
27 making them promising candidates for energy storage applications. For example, Naderi *et al.*  
28 demonstrated that CoWO<sub>4</sub>/nitrogen-doped reduced graphene oxide (CoWO<sub>4</sub>/NRGO) sheets  
29 exhibit a high specific capacitance of 597 F g<sup>-1</sup> at 5 mV s<sup>-1</sup> in a 2 M H<sub>2</sub>SO<sub>4</sub> electrolyte, with  
30 only a 2.9% decay after 4000 cycles.<sup>35</sup> Similarly, Sohoulou *et al.* synthesized nanosphere-like  
31 MnO<sub>2</sub>/CoWO<sub>4</sub>/NCNO via a hydrothermal method and reported a specific capacitance of 536  
32 F g<sup>-1</sup> at 2 A g<sup>-1</sup> in a 6 M KOH electrolyte, demonstrating excellent suitability for SC  
33 applications.<sup>36</sup> Even though metal-tungstate-based electrode materials have advanced, their



1 poor electrical conductivity and limited surface area limit their practical applications.  
2 Henceforth, to improve the charge transport and electroactive surface sites. Hence, we report a  
3 facile one-pot strategy for the preparation of a ternary oxide SrWO<sub>4</sub>/rGO nanocomposite via a  
4 reaction between Na<sub>2</sub>WO<sub>4</sub>·2H<sub>2</sub>O, SrCl<sub>2</sub>·6H<sub>2</sub>O, and rGO dispersion. Nanocrystalline SrWO<sub>4</sub> on  
5 rGO was formed via a simple, low-temperature hydrothermal process that exploits SrWO<sub>4</sub>'s  
6 electrochemically active sites while suppressing rGO restacking, thereby enhancing  
7 electrochemical performance. As expected, the SrWO<sub>4</sub>/rGO electrode exhibited excellent SC  
8 performance, characterized by high specific capacitance, outstanding cycling stability, and  
9 remarkable reversibility. These enhanced properties are attributed to the material's improved  
10 electrical conductivity, shortened ion diffusion pathways, and the direct integration of the  
11 active material onto a conductive substrate.

## 12 2. Experimental Section

### 13 2.1. Synthesis of SrWO<sub>4</sub> Nanospheres

14 All reagents and chemicals utilized were of analytical grade and do not require further  
15 purification. The hydrothermal method was employed to synthesise strontium tungstate  
16 nanospheres, with minor modifications relative to our previous reports.<sup>20</sup> The materials were  
17 dissolved and recrystallized in solvents under elevated temperatures and pressures.<sup>37</sup>  
18 Specifically, 30 mL of deionized (DI) water was utilized to separately dissolve 1.3 g of  
19 Na<sub>2</sub>WO<sub>4</sub>·2H<sub>2</sub>O and 1.0 g of SrCl<sub>2</sub>·6H<sub>2</sub>O. During ultrasonication, the SrCl<sub>2</sub>·6H<sub>2</sub>O solution was  
20 gradually added dropwise into the Na<sub>2</sub>WO<sub>4</sub>·2H<sub>2</sub>O mixture. The resulting homogeneous  
21 solution was then securely sealed and ultrasonically agitated for 1hr at room temperature. A  
22 few drops of HCl or NaOH were added to stabilize pH fluctuations. After continuous agitation  
23 using a magnetic stirrer, the reaction solution was moved to a stainless-steel autoclave and kept  
24 at 120 °C for 12 h. A white precipitate was formed at the end of the process. After  
25 centrifugation, the precipitate was carefully washed with ethanol and DI water and dried for 12  
26 h at 80 °C. Lastly, a muffle furnace was used to calcine the SrWO<sub>4</sub> powder for 3 h at 300 °C.

### 27 2.2 Synthesis of SrWO<sub>4</sub>/rGO Nanocomposite:

28 Graphene Oxide (GO) was synthesized using the controlled Hummers' method.<sup>2</sup>  
29 SrWO<sub>4</sub>/rGO nanocomposites were synthesized via a one-pot, hydrothermal process. Initially,  
30 60 mL of DI water was utilized to disperse 0.02 g of GO powder, followed by ultrasonication  
31 for 2h to remove any unexfoliated GO. The obtained exfoliated GO (EGO) was then dried at



1 45 °C for 24 h. Subsequently, 100 mg of EGO was dispersed in 400 mL of distilled water under  
2 continuous stirring and heated at 95 °C for 4 days to obtain a stable, clear, light-brown rGO  
3 suspension. Afterwards, 1.3 g of Na<sub>2</sub>WO<sub>4</sub>·2H<sub>2</sub>O and 1.0 g of SrCl<sub>2</sub>·6H<sub>2</sub>O were added to the  
4 rGO dispersion and stirred for an additional 2 h. A few drops of HCl or NaOH were added to  
5 stabilize pH fluctuations. The resultant mixture was autoclaved at 120 °C for 12 h, and the  
6 resulting white precipitate was centrifuged and washed with ethanol and DI water. Finally, the  
7 black precipitate was vacuum dried for 8 h at 80 °C. Lastly, a muffle furnace was used to  
8 calcine the SrWO<sub>4</sub> powder for 3 h at 300 °C, yielding a stable SrWO<sub>4</sub>/rGO nanocomposite.  
9 Schematic illustration of the hydrothermal synthesis of SrWO<sub>4</sub>/rGO nanocomposite, and  
10 Electrochemical analysis with GCD and Specific capacitance curves. (Scheme 1).

### 11 2.3 Electrode Fabrication and Characterisation

12 The following procedure was employed to fabricate the modified electrodes and to  
13 perform electrochemical analyses at room temperature. The electroactive materials (SrWO<sub>4</sub>,  
14 rGO, and SrWO<sub>4</sub>/rGO), the binder (polyvinylidene fluoride, PVDF), and the conductive carbon  
15 black were thoroughly mixed in a 8:1:1 ratio. Then, 10 μL of NMP (N-Methyl-2-pyrrolidone)  
16 was added to the powder mixture to form a viscous slurry. The slurry was coated onto a 1 × 1  
17 cm<sup>2</sup> nickel foam (NF) substrate, which served as the working electrode, and dried in a hot air  
18 oven at 60 °C.<sup>2</sup> Electrochemical studies were performed using a symmetrical two-electrode SC  
19 (STS) with SrWO<sub>4</sub>/rGO/NF as both electrodes, PVA/KOH gel as the electrolyte, and a  
20 microfiber glass filter (0.18 mm thick) as the separator. Electrochemical impedance  
21 spectroscopy (EIS), galvanostatic charge-discharge (GCD), and cyclic voltammetry (CV)  
22 measurements were performed using a CHI 760E electrochemical workstation in a three-  
23 electrode configuration, consisting of platinum wire (counter electrode), saturated Ag/AgCl  
24 (reference electrode), and SrWO<sub>4</sub>, rGO, and SrWO<sub>4</sub>/rGO (working electrode). The mass of the  
25 active material loaded onto the fabricated electrode was 3 mg. The specific capacitance (C<sub>sp</sub>)  
26 was calculated from galvanostatic charge-discharge (GCD) curves using Eq. (1).<sup>38, 39</sup>

$$27 \quad C_s = I \times \Delta t / m \times \Delta V \times (F g^{-1}) \quad (1)$$

28 where m represents the mass of the active material (mg), ΔV denotes the potential window  
29 (V), I corresponds to the discharge current (A), and Δt is the discharge time (s).

### 30 3. Results and Discussion



### 1 3.1 Investigation of Crystallinity, Functional Groups, and Lattice Vibrations of the 2 Synthesized Materials

3 The crystallization of SrWO<sub>4</sub> and its interaction with rGO occurred simultaneously during the  
4 process.<sup>28</sup> **X-ray diffraction (XRD)** was performed to evaluate the phase composition and  
5 crystallinity of the synthesized materials. SrWO<sub>4</sub> crystallizes in the tetragonal I4<sub>1</sub>/a space group  
6 and has a structure similar to zircon. Sr<sup>2+</sup> ions are coordinated by eight equivalent O<sup>2-</sup> ions,  
7 forming an eightfold (eight-coordinate) coordination geometry. W<sup>6+</sup> ions are coordinated by  
8 four equivalent O<sup>2-</sup> ions, forming a tetrahedral coordination geometry. Each O<sup>2-</sup> ion is  
9 threefold coordinated, bonding to two equivalent Sr<sup>2+</sup> ions and one W<sup>6+</sup> ion, as illustrated in  
10 **Fig. 1. (a)**. The tetrahedral scheelite-type crystal structure of SrWO<sub>4</sub>, analogous to that of  
11 zircon, underpins its electrochemical performance in a SC by providing a framework of  
12 coordinated polyhedra that facilitates redox reactions and ion transport dynamics. (Data  
13 retrieved from the Materials Project for SrWO<sub>4</sub> (mp-19163) from database version  
14 v2025.09.25.) In addition, the distorted eight-coordinate geometry of Sr<sup>2+</sup> improves lattice  
15 stability and ion diffusion pathways, thereby facilitating electrolyte accessibility and ion  
16 diffusion, while the tetrahedral WO<sub>4</sub> units act as electrochemically active centres that enable  
17 Faradaic redox reactions involving the W<sup>6+</sup>/W<sup>5+</sup> redox couple, contributing to pseudo-  
18 capacitance.<sup>11</sup> In this crystal system, each W<sup>6+</sup> ion is tetrahedrally coordinated by four oxygen  
19 ions forming isolated [WO<sub>4</sub>]<sup>2-</sup> units, while Sr<sup>2+</sup> ions occupy eight-fold coordination; this  
20 structural arrangement gives rise to structural disorder and oxygen vacancies, which create  
21 localized electronic energy levels and additional active sites. In addition, the presence of W<sup>6+</sup>  
22 and W<sup>5+</sup> enables reversible faradaic redox transitions, thereby improving overall  
23 electrochemical performance.<sup>40</sup> Pristine SrWO<sub>4</sub> typically shows clear and well-defined  
24 diffraction peaks matching its tetragonal scheelite structure, indicating a substantially bigger  
25 crystallite size and higher crystallinity index, combined with lower micro strain and dislocation  
26 density due to its well-ordered lattice (**Table S1**). This is evidenced by the Rietveld refinement  
27 **Fig. 1. (b)**, where the observed XRD pattern and the theoretically calculated pattern exhibit  
28 minimal deviation, and both profiles are well aligned with the corresponding Bragg Positions.  
29 **Fig. 2. (a)** presents the comparative stacked XRD patterns for pure SrWO<sub>4</sub>, rGO, and the  
30 SrWO<sub>4</sub>/rGO composite. The pattern of pure SrWO<sub>4</sub>, **Fig. 2. (a), red curve** shows characteristic  
31 peaks at (112) plane 27.41° and (004),(200)planes 29.8°, 32.9°, displaying sharp and  
32 intense peaks, confirming its crystalline nature. These peaks match well with the JCPDS card  
33 number 01-089-2568.<sup>32</sup> No secondary peaks were observed, indicating that the synthesized



1 SrWO<sub>4</sub> has high phase purity. On the other hand, rGO exhibits a broad, weak diffraction peak, typically around the (002) plane, indicative of higher lattice distortion, smaller effective crystallite domains, poor long-range order, and, consequently, increased microstrain and dislocation density. Strong interfacial interactions between SrWO<sub>4</sub> and rGO result in a considerable decrease in crystallite size and crystallinity, as indicated by the XRD peaks of SrWO<sub>4</sub>/rGO, which remain intact but somewhat widened and decreased in intensity upon composite formation, as shown in **Table S1**. This interaction introduces additional lattice strain and defects, as evidenced by higher microstrain and dislocation density compared to pure SrWO<sub>4</sub>. In general, the composite structure strikes a compromise between defect density and crystallinity, which is advantageous for improved electrochemical performance. The XRD analysis of rGO shows two characteristic peaks at 13.18° and 26.68° as shown in **Fig. 2. (a), black curve**, which correspond to the (100) and (002) crystal planes associated with intraplanar and inter-planar aromatic stacking, respectively, in accordance with JCPDS card number 01-087-1526.<sup>29</sup> Meanwhile, the XRD pattern of the SrWO<sub>4</sub>/rGO composite (**Fig. 2. (a), blue curve**) reveals no additional or separate crystalline phases. Still, the presence of the rGO (002) peak is clearly evident. Importantly, all characteristic diffraction planes of SrWO<sub>4</sub> are also present in the composite, indicating the successful formation of a binary heterojunction structure between SrWO<sub>4</sub> and rGO. Furthermore, the crystallite size and microstrain ( $\epsilon$ ) of SrWO<sub>4</sub> and SrWO<sub>4</sub>/rGO were assessed using the Williamson–Hall (W–H) plot. The W–H plots for SrWO<sub>4</sub> and SrWO<sub>4</sub>/rGO are presented as  $4\sin\theta$  versus  $\beta\cos\theta$  in Fig. S5(c,d). The microstrain ( $\epsilon$ ) is obtained from the slope of the linear fit, while the crystallite size is determined from the intercept ( $k\lambda/D$ , where  $k = 0.9$ ).<sup>41, 42</sup> According to the Scherrer and W-H methods, the average crystallite sizes of SrWO<sub>4</sub> and SrWO<sub>4</sub>/rGO are 30.33 nm and 57.44 nm, respectively. The positive microstrain value ( $\epsilon = 2.22 \times 10^{-3}$ ) indicates the presence of tensile lattice strain. Upon composite formation with rGO, the tetragonal structure of SrWO<sub>4</sub> is retained. At the same time, the conductive rGO network provides rapid electron transport pathways to the redox-active [WO<sub>4</sub>]<sup>2-</sup> units, prevents aggregation of SrWO<sub>4</sub> particles, and ensures uniform dispersion of the active phase. As a result, the SrWO<sub>4</sub>/rGO composite achieves a synergistic combination of EDLC from rGO and greatly amplified pseudocapacitance from the tetrahedrally coordinated SrWO<sub>4</sub>, yielding superior specific capacitance compared to either individual component, while maintaining excellent structural stability and cycling performance owing to the robust tetragonal scheelite framework.



1 **Fourier Transform Infrared Spectroscopy (FT-IR)** analysis confirmed the chemical bonds  
 2 and functional groups present in SrWO<sub>4</sub>, rGO, and SrWO<sub>4</sub>/rGO composite, as evidenced from  
 3 the stacked comparative FT-IR spectrum, **Fig. 2. (b)**, **red curve** in **Fig. 2. (b)** represents the  
 4 spectrum of SrWO<sub>4</sub>, bands at 415 and 789  $cm^{-1}$  indicate the presence of Sr and W elements,  
 5 typical of SrWO<sub>4</sub>.<sup>18</sup> While peaks at 866 and 679  $cm^{-1}$  represent  $W-O$  and  $W-O-W$   
 6 vibrations. Whereas 1124  $cm^{-1}$  band confirms the presence of  $WO_4^{2-}$  groups.<sup>22</sup> Thus, the  $W$   
 7  $O_4^{2-}$  vibrations represent intact tetrahedra, which facilitate  $W^{6+}/W^{5+}$  redox-faradaic reactions;  
 8 this inference aligns with XRD reports.<sup>34</sup> **black curve** in **Fig. 2. (b)** represents rGO's spectrum,  
 9 which exhibits characteristic absorption bands that appear at 1538  $cm^{-1}$  - corresponding to  
 10 carbonyl groups of carboxylic derivatives, 1225  $cm^{-1}$  - corresponding to  $C=C$  stretching  
 11 of aromatic rings, and 1084  $cm^{-1}$  - corresponding to the  $C-OH$  stretching vibrations.  
 12 Presence of  $-OH$  and  $C=O$  in the rGO increases the conductivity and enables rapid ion  
 13 adsorption.<sup>43</sup> The absorption peaks at 3537 and 1640  $cm^{-1}$  correspond to  $-OH$  stretching  
 14 and H<sub>2</sub>O bending vibrations, respectively.<sup>39</sup> The FTIR spectrum of SrWO<sub>4</sub>/rGO (**Fig. 2. (b)**,  
 15 **blue curve**) displays the characteristic peaks of both SrWO<sub>4</sub> and rGO. The bands near 3395  
 16  $cm^{-1}$  ( $-OH$  stretching) and 1401  $cm^{-1}$  (H<sub>2</sub>O bending vibrations), have obtained a slight  
 17 negative shift, confirming the effective reduction of rGO in the composite.<sup>44</sup> These changes in  
 18 the absorption bands support the fact that SrWO<sub>4</sub> is embedded over the rGO sheets, indicating  
 19 SrWO<sub>4</sub> aligns with the XRD results.

20 Subsequently, the structural vibrations of the materials were analyzed using Raman  
 21 spectroscopy, as illustrated in the stacked comparative spectrum in **Fig. 2. (c)**. The **Raman**  
 22 **spectrum** of SrWO<sub>4</sub> displays distinct bands at 327, 365, 794, 827, and 913  $cm^{-1}$ ,  
 23 corresponding to the  $\nu_2(Ag)$ ,  $\nu_4(Bg)$ ,  $\nu_2(Eg)$ ,  $\nu_3(Bg)$ , and  $\nu_1(Ag)$  vibrational modes,  
 24 consistent with previous reports.<sup>41</sup> The band at 180  $cm^{-1}$  corresponds to the tetrahedral  $W$   
 25  $O_4^{2-}$  unit, as shown in **Fig. 2. (c)**, **red curve**.<sup>23</sup>  $\nu_1(Ag)$  vibrational mode at 913  $cm^{-1}$   
 26 represents tetrahedral rigidity for stable  $W^{6+}/W^{5+}$  redox during charge-discharge cycles.<sup>11</sup> In  
 27 the rGO spectrum (**Fig. 2. (c)**, **black curve**), the characteristic D and G bands appear at 1398  
 28  $cm^{-1}$  and 1558  $cm^{-1}$ , corresponding to defect-induced vibrations ( $sp^3$  carbon) and the in-  
 29 plane  $E_{2g}$  mode of  $sp^2$  carbon, respectively. This is consistent with our previous results, where  
 30 GO exhibited similar D and G bands at  $\sim 1336$  and  $\sim 1595$   $cm^{-1}$ .<sup>2</sup> The intensity ratio ( $I_D/I_G$ ), a  
 31 key indicator of structural disorder and reduction, increases from 0.83 for GO to 0.897 for  
 32 rGO, confirming the effective removal of oxygen functional groups and partial restoration of



1 the  $sp^2$  carbon network. This increase is attributed to the formation of smaller, yet more  
 2 numerous graphitic domains, which enhances defect-related scattering. Furthermore, the  
 3 Raman spectrum of the  $SrWO_4/rGO$  composite displays all characteristic modes of the  
 4 individual components, with slight shifts toward lower wavenumbers, indicating strong  
 5 interfacial interactions. The  $I_D/I_G$  ratio in the composite further increases to 0.9–1.02, likely  
 6 due to bond formation between rGO sheets and Sr/W ions. These results confirm the successful  
 7 synthesis of the  $SrWO_4/rGO$  composite.<sup>45</sup>

8 The optical properties of the  $SrWO_4$ , rGO, and  $SrWO_4/rGO$  samples were analyzed using **UV-**  
 9 **Visible spectroscopy**. As it's typical for scheelite-type inorganic phases, the UV absorption  
 10 spectrum of  $SrWO_4$  (**Fig. S1, red curve**) exhibits a significant absorption peak at 360 nm,  
 11 attributed to the  $WO_4^{2-}$  group.<sup>42</sup> The absorption band centred at 297 nm in rGO, shown in  
 12 **Fig. S1. - black curve**, is due to the  $\pi - \pi^*$  transitions of the  $\pi$  bonds in graphene, indicating  
 13 the successful reduction of GO to rGO.<sup>27</sup> As shown in **Fig. S1. - blue curve**, the absorbance  
 14 intensity of  $SrWO_4/rGO$  is shifted to a longer wavelength compared to that of rGO. This  
 15 observed red shift in  $SrWO_4/rGO$  is attributed to electron-hole transitions between  $SrWO_4$  and  
 16 rGO.<sup>45</sup>

### 17 **3.2. XPS, BET Surface Area, Morphology, and Particle Size Analysis**

18 Subsequently, XPS analysis was conducted to examine the atomic and chemical constituents  
 19 of the materials ( $SrWO_4/rGO$ ). The XPS survey spectrum, along with the chemical composition  
 20 shown in **Fig. 3. (a)**, confirms the presence of elements such as Sr, W, C, and O. The core-level  
 21 spectrum of Sr 3d (**Fig. 3. (b)**) exhibits two distinct peaks at 134.8 and 133.2 eV, for the  $3d_{3/2}$   
 22 and  $3d_{5/2}$  spin-orbit levels.<sup>24</sup> These symmetric doublets confirm the stability of  $Sr^{2+}$  in 8-  
 23 coordinate polyhedra, which facilitates structural stability and electrolyte access.<sup>11</sup> In **Fig. 3.**  
 24 **(c)**, the W 4f, the spectrum reveals prominent peaks at 38.41 eV and 35.7 eV for W  $4f_{5/2}$  and W  
 25  $4f_{7/2}$ , confirming tungsten in the  $W^{6+}$  oxidation state.<sup>46, 47</sup> This validates tetrahedral integrity for  
 26 reversible faradaic redox ( $W^{6+}/W^{4+}$ ) in charge discharge cycles.<sup>48</sup> The core-level spectrum of  
 27 O 1s shows two deconvoluted peaks. As illustrated in **Fig. 3. (d)**, the peaks located at 532.6  
 28 and 530.8 eV correspond to metal-oxygen ( $M - O$ ) bonds such as  $W - O$  and  $Sr - O$ , and to  
 29 chemisorbed oxygen originating from surface hydroxyl groups, respectively.<sup>10</sup> These enhance  
 30 hydrophilicity, thereby confirming electrolyte wetting.<sup>49</sup> Furthermore, the C 1s spectrum in  
 31 **Fig. 3. (e)** displays three distinct binding energy peaks at 284.9, 286.3, and 288.6 eV, which



1 are attributed to aromatic carbon species, namely,  $C = C$ ,  $C - O$ ,  $O - C = O$  functional groups,  
2 indicating effective GO removal. These results are consistent with previous studies.<sup>50</sup> The XPS  
3 measurements confirmed the successful synthesis of a highly pure and crystalline  $SrWO_4/rGO$   
4 composite. Due to the synergistic effect of the synthesized  $SrWO_4/rGO$ , it has potential as an  
5 electrochemically active material for SC applications. XRD, Raman spectroscopy, and XPS  
6 were used in a mutually confirming framework for the structural analysis of pristine  $SrWO_4$ ,  
7 pure rGO, and  $SrWO_4/rGO$  composite. The crystalline phase, lattice structure, and crystallite  
8 size are the main information revealed by XRD. For instance, the formation of crystalline  
9  $SrWO_4$  is confirmed by well-defined diffraction peaks. In contrast, any broadening or  
10 decreased intensity indicates decreased crystallinity or structural disorder after cycling. This is  
11 further supported by Raman spectroscopy, which examines carbon-related structural features,  
12 particularly the D and G bands, which reveal information about defect density and  
13 graphitisation; a greater  $I_D/I_G$  ratio usually indicates the reduction of GO to rGO and higher  
14 defect sites that boost electrochemical activity. On the other hand, XPS confirms the effective  
15 formation of the composite by providing surface-sensitive chemical information that identifies  
16 elemental composition and oxidation states (e.g.,  $W^{6+}$ ,  $Sr^{2+}$ , and  $C-C/C-O$  bonding). Together,  
17 these findings show that the synergistic combination of crystalline metal oxide frameworks and  
18 defect-rich conductive carbon networks leads to improved SC performance.<sup>40</sup> Overall, the  
19 results from XRD, Raman, and XPS are in good agreement, collectively confirming the  
20 structural integrity, vibrational characteristics, and surface chemical composition of the  
21 composite, which supports its enhanced electrochemical performance.

22 The  $N_2$  adsorption-desorption isotherm curves (**Fig. 3. (f)**) were employed to evaluate the  
23 specific surface area and pore diameter of the  $SrWO_4/rGO$  composite. Optimal pore diameter  
24 and ideal specific surface area are essential for electrode materials to achieve maximum  
25 capacitive performance. The type IV hysteresis loops (**Fig. 3. (f), inset**) reveal numerous  
26 mesopores in the hybrid structure, resulting from the integration of rGO nanosheets.<sup>51</sup> The  
27  $SrWO_4/rGO$  hybrid structure has a specific surface area of  $19\ m^2\ g^{-1}$ . The BJH (Barrett-  
28 Joyner-Halenda) analysis confirms that the  $SrWO_4/rGO$  hybrid structure is mesoporous, with  
29 a pore-size distribution centred at  $35.54\ \text{\AA}$  and a pore volume of  $0.1158\ cm^3\ g^{-1}$ . Due to their  
30 mesoporous structure and large surface area,  $SrWO_4/rGO$  nanocomposites enhance  
31 electrochemical performance by improving electrode-electrolyte interactions during the  
32 reaction.<sup>7</sup>



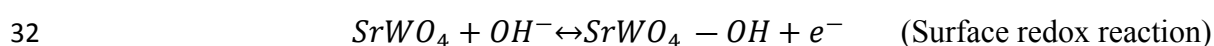
1 HR-SEM analysis was used to investigate the structure and surface morphology of  
2 SrWO<sub>4</sub>, rGO, and SrWO<sub>4</sub>/rGO composites. HR-SEM images at various magnifications (**Fig.**  
3 **4. (a-c)**) show that bare SrWO<sub>4</sub> nanoparticles have a spherical-like structure. The HR-SEM  
4 images of rGO at various magnifications (**Fig. 4. (d-f)**) reveal scrolled, rippled, and wrinkled  
5 features, indicating a large surface area.<sup>52</sup> (**Fig. 4. (g-i)**) illustrates the distorted spherical  
6 SrWO<sub>4</sub> particles embedded within the rGO composite, highlighting the morphological features  
7 of the synthesized SrWO<sub>4</sub>/rGO composite.

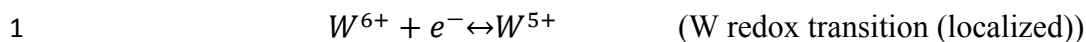
8 HR-TEM was employed to further the morphological features and size of the  
9 synthesized SrWO<sub>4</sub>, rGO, and SrWO<sub>4</sub>/rGO nanocomposite (**Fig. 5**). The HR-TEM images of  
10 pure SrWO<sub>4</sub> reveal distorted and dispersed spherical nanoparticles (**Fig. 5. (a-b)**). The material  
11 exhibits a high specific surface area and excellent flexibility, resulting in a crumpled structure.  
12 At the same time, interlayer attraction causes a slight stacking of rGO layers. **Fig. 5. (c)** shows  
13 that the layered rGO structure typically consists of translucent, sheet-like regions interspersed  
14 with wrinkled or folded areas. Electrostatic interactions play a key role in the synthesis process.  
15 After adding SrCl<sub>2</sub>, the negatively charged rGO sheets strongly adsorb the Sr<sup>2+</sup> ions. The  
16 addition of tungstate salt (Na<sub>2</sub>WO<sub>4</sub>) increases the solution's positive charge, promoting the  
17 adsorption of WO<sub>4</sub><sup>2-</sup> anions.<sup>20, 32</sup> The SrWO<sub>4</sub> particles strongly adhere to the rGO sheets,  
18 forming a well-integrated SrWO<sub>4</sub>/rGO composite, as shown in **Fig. 5. (d-f)**. High-resolution  
19 TEM images illustrate the arrangement of atomic planes in SrWO<sub>4</sub> (**Fig. 5. (b)**) and rGO (**Fig.**  
20 **5. (c)**) through the lattice fringes, with their respective interplanar length of 0.457 nm (**Fig. 5.**  
21 **(g)**). Unlike the rest of the sheet, the SrWO<sub>4</sub> particles typically appear as black patches. Pure  
22 crystallinity of the produced SrWO<sub>4</sub>/rGO nanocomposite is shown by the bright circular rings  
23 seen in the SAED pattern (**Fig. 5. (h)**). Additionally, as shown in **Fig. 5. (i)**, the SrWO<sub>4</sub>/rGO  
24 composite contained the expected Elements C, O, Sr and W. The EDX spectrum confirmed  
25 that the composite was free of contaminants. EDS (EDAX) analysis verifies the elemental  
26 composition, showing weight percentages of C (11.0 wt%), O (41.8 wt%), Sr (11.8 wt%), and  
27 W (35.4 wt%), demonstrating the presence of all expected elements and confirming the  
28 successful formation of the SrWO<sub>4</sub>/rGO nanocomposite. The corresponding weight  
29 percentages of C (32.29 wt%), O (39.62 wt%), Sr (8.18 wt%), and W (19.92 wt%) and atomic  
30 percentages of C (50.09 wt%), O (46.15 wt%), Sr (1.74 wt%), and W (2.02 wt%) further  
31 support the successful formation of the SrWO<sub>4</sub>/rGO nanocomposite (**Fig. 5. (I, inset)**).

### 32 3.3 Electrochemical Performance of the SrWO<sub>4</sub>/rGO Composite



1 The electrochemical performance of the samples was tested in a 3-electrode system using 1 M  
 2 KOH as the electrolyte. To evaluate the electrochemical performance, CV and GCD  
 3 measurements of SrWO<sub>4</sub> (red curve) and SrWO<sub>4</sub>/rGO (blue curve) were carried out at a scan  
 4 rate of 50 mV s<sup>-1</sup> and a current density of 1 A g<sup>-1</sup>, as shown in **Fig. S2. (a-b)**. CV profiles of  
 5 SrWO<sub>4</sub> exhibited quasi-rectangular curves with broad redox peaks at ~0.4–~0.55 V vs  
 6 Ag/AgCl, corresponding to the W<sup>6+</sup>/W<sup>5+</sup> redox reaction. In contrast, these CV loops expand  
 7 for SrWO<sub>4</sub>/rGO with higher capacitance at higher scan rates, indicating rapid ion adsorption  
 8 on rGO sheets with a sustained W<sup>6+</sup>/W<sup>5+</sup> redox couple.<sup>53,54</sup> This CV and GCD profiles indicate  
 9 that both SrWO<sub>4</sub>/rGO exhibit pseudocapacitive behaviour. The smallest integral area in the  
 10 diagram corresponds to the lowest energy storage capacity. At the same time, the composite's  
 11 simultaneously highest current magnitude indicates that the SrWO<sub>4</sub>/rGO hybrid outperforms  
 12 both SrWO<sub>4</sub> and rGO. According to the BET analysis (**Fig. 3. (f)**), the high surface area of  
 13 SrWO<sub>4</sub>/rGO improves ion diffusion and likely enhances performance by increasing the number  
 14 of available ion adsorption sites. The Faradaic reactions associated with the pseudo-capacitance  
 15 effect give rise to redox peaks in the CV and GCD of SrWO<sub>4</sub>/rGO/NF at 50 mV s<sup>-1</sup> (**Fig. S2.**  
 16 **(a-b), blue curve**). In SrWO<sub>4</sub>/NF, tungsten primarily enhances SrWO<sub>4</sub>'s conductivity, thereby  
 17 improving the overall electrochemical capacitance.<sup>55</sup> The CV curves of SrWO<sub>4</sub>/NF and  
 18 SrWO<sub>4</sub>/rGO/NF were tested at scan rates (v) of 10 to 100 mV s<sup>-1</sup> within 0 to 0.7 V (**Fig. 6.**  
 19 **(a-b)**). The Faradaic mechanism consistently exhibited characteristic pseudocapacitive  
 20 behaviour, as reflected in the quasi-rectangular shape of the CV curves.<sup>22</sup> Each CV curve shows  
 21 strong electrochemical reversibility, with nearly symmetrical, well-defined redox peaks,  
 22 indicating faster redox kinetics for the redox couple (W<sup>6+</sup>/W<sup>5+</sup>). **Fig. 6. (b)** shows the CV  
 23 profile of SrWO<sub>4</sub>/rGO, where the carbon in the rGO and bimetallic components (SrWO<sub>4</sub>)  
 24 contribute to the increased capacitance observed in the composite's integrated area. Peak  
 25 current rises with scan rate, indicating diffusion-controlled redox at the electrode. An  
 26 increment in the scan rate shifts cathodic peaks to higher potential and anodic peaks to lower  
 27 potentials.<sup>53</sup> The reaction mechanism is associated with the interaction of SrWO<sub>4</sub> with  
 28 hydroxide ions, while the [WO<sub>4</sub>]<sup>2-</sup> groups provide structural stability. The presence of rGO  
 29 improves the electrical conductivity and facilitates ion transport. When the SrWO<sub>4</sub> electrode is  
 30 immersed in a KOH electrolyte, the following surface reaction occurs, while W does not  
 31 directly participate in the faradaic reactions:<sup>56-58</sup>





2 The overall capacitance of SrWO<sub>4</sub>/NF and SrWO<sub>4</sub>/rGO/NF comprises surface-controlled  
3 capacitance, including reversible double-layer and surface redox pseudo-capacitance, as well  
4 as diffusion-controlled capacitance. SrWO<sub>4</sub>/rGO/NF outperformed several reported materials  
5 listed in **Table S4**. Eq. (2) and (3) are used to further evaluate the nanocomposite's  
6 electrochemical performance by applying the power law, relating current density (*j*) to scan  
7 rate (*v*):<sup>2, 59</sup>

$$8 \quad j = av^b \quad (2)$$

$$9 \quad j = k_1v = k_2v^{\frac{1}{2}} \quad (3)$$

10 Here, *v* and *j* represent scan rate and current density, respectively, while *k*<sup>1</sup>, *k*<sup>2</sup>, are constant,  
11 and both *a* and *b* are adjustable parameters.

12 The slope value (*b* = 1) denotes a capacitive contribution mechanism, whereas the slope  
13 value of (*b* = 0.5) denotes diffusion-controlled contribution to charge storage. The capacitive  
14 contribution (Dunn method) of SrWO<sub>4</sub>/NF (**Fig. S4. (a-d)**) and SrWO<sub>4</sub>/rGO/NF (**Fig. 7. (a-d)**)  
15 decreases at 10 *mV s*<sup>-1</sup> and increases to 100 *mV s*<sup>-1</sup>. According to **Fig. 7. (b)** and **S4. (b)**, the  
16 calculated slope value (*b*) from anodic peak currents in 1 M KOH is approximately 0.636 *A*  
17 for SrWO<sub>4</sub>/NF and 0.641 *A* for SrWO<sub>4</sub>/rGO/NF. This suggests that both diffusion-controlled  
18 and capacitive mechanisms drive the reaction.<sup>10</sup> Furthermore, **Fig. 7. (c)** and **S4. (c)** illustrate  
19 the capacitive and diffusive charge contributions of SrWO<sub>4</sub>/NF and SrWO<sub>4</sub>/rGO/NF,  
20 respectively. The results reveal that the capacitive contribution increases with the scan rate,  
21 ranging from 59% to 82% for SrWO<sub>4</sub>/NF and 86% to 95% for SrWO<sub>4</sub>/rGO/NF as the scan  
22 rate increases from 10 to 100 *mV s*<sup>-1</sup>. Moreover, **Fig. 7. (d)** and **S4. (d)** plots of the *i*<sub>p</sub> versus  
23 √*v* for SrWO<sub>4</sub>/NF and SrWO<sub>4</sub>/rGO/NF. With anodic and cathodic peak correlation coefficients  
24 (*R*<sup>2</sup>) of 0.97 for SrWO<sub>4</sub>/NF and 0.99 for SrWO<sub>4</sub>/rGO/NF, the results indicate that the electrode  
25 response is predominantly diffusion-controlled.<sup>60</sup> The capacitance of SrWO<sub>4</sub>/NF and  
26 SrWO<sub>4</sub>/rGO/NF materials was evaluated using GCD tests at 1 *A g*<sup>-1</sup>, as demonstrated in **Fig.**  
27 **S2. (b)**. Notably, SrWO<sub>4</sub>/rGO/NF exhibits the most prominent charge/discharge plateau in the  
28 GCD curves, which is attributed to its excellent free-electron transport during electrochemical  
29 processes, ensuring efficient electron transfer. Likewise, the GCD curves at 1 – 10 *A g*<sup>-1</sup>  
30 reveal high electrochemical reversibility and capacitance for both SrWO<sub>4</sub>/NF (**Fig. 6. (c)**) and  
31 SrWO<sub>4</sub>/rGO (**Fig. 6. (d)**) SC electrodes. To further understand the charge transfer and ion  
32 diffusion behaviour, EIS was performed for the SrWO<sub>4</sub>, rGO, and SrWO<sub>4</sub>/rGO electrodes in



1 1 M KOH over the frequency range of 10 mHz to 100 kHz. As shown in Fig. 8. (a), the  
2 Nyquist plots with a high-frequency semicircle and a low-frequency vertical line indicate that  
3 the synergistic interaction between SrWO<sub>4</sub> and rGO improves both electrical conductivity and  
4 charge storage capability.<sup>61</sup> The semicircle diameter represents the interfacial charge transfer  
5 resistance ( $R_{ct}$ ) which is influenced by Faradaic processes and double-layer Capacitance ( $C_{dl}$ ).  
6 The corresponding data were fitted using a Randles equivalent circuit comprising the solution  
7 resistance ( $R_s$ ), charge-transfer resistance ( $R_{ct}$ ), double-layer capacitance ( $C_{dl}$ ), and Warburg  
8 impedance ( $Z_w$ ).<sup>62</sup> The charge transfer kinetics and frequency response behaviour of the  
9 SrWO<sub>4</sub>/rGO composite were thoroughly assessed using EIS in both three-electrode and two-  
10 electrode configurations. The Nyquist plot of rGO and SrWO<sub>4</sub>/rGO in the three-electrode  
11 system shows a small compressed semicircle with  $R_s = 0.8 \Omega$  and  $R_{ct} = 2.2 \Omega$ , and  $R_s = 1.3 \Omega$   
12 and  $R_{ct} = 4.8 \Omega$ , indicating reductions compared to pristine SrWO<sub>4</sub> ( $R_s = 4.2 \Omega$ ,  $R_{ct} = 15.3 \Omega$ ).  
13 (inset of Fig. 8. (a)). The fitted parameters are summarized in Table S2. This confirms that the  
14 rGO conductive network significantly reduces both ohmic and kinetic resistances at the  
15 material level. In comparison to SrWO<sub>4</sub> ( $\tau_0 = 5.88$  s) and rGO ( $\tau_0 = 2.22$  s), the comparable  
16 Bode phase diagram for SrWO<sub>4</sub>/rGO produces  $f_0 = 1.16$  Hz and  $\tau_0 = 0.86$  s, indicating quicker  
17 charge-discharge kinetics due to the additional contributions of separator ionic resistance, dual  
18 electrode interfaces, and the entire electrolyte bulk path. The EIS parameters in the two-  
19 electrode symmetric device configuration show the anticipated increase:  $R_s = 1.3 \Omega$  and  $R_{ct} =$   
20  $4.2 \Omega$ . This is consistent with reports for similar symmetric SC devices, where two-electrode  
21  $R_s$  and  $R_{ct}$  values are higher than those for three-electrode devices.<sup>10</sup> Extracted from the two-  
22 electrode Bode phase plot, the device-level relaxation time constant (2E)  $\tau_0 = 1.18$  s ( $f_0 = 0.85$   
23 Hz) is competitive with similar tungstate-based composite devices, indicating that the practical  
24 device maintains the fast kinetic advantages imparted by the rGO scaffold. The superior  
25 charge-transport characteristics of the SrWO<sub>4</sub>/rGO composite for high-performance SC  
26 applications are confirmed by a systematic comparison of EIS parameters between the two  
27 configurations, which provides a comprehensive kinetic picture that separates the intrinsic  
28 material response (three electrodes) from the practical device performance. Notably, the  
29 SrWO<sub>4</sub>/rGO electrode shows the lowest  $R_{ct}$ , indicating more efficient electron transport and  
30 faster interfacial charge transfer. Fig. S5. (c-d) presents the Bode plots (phase angle and total  
31 impedance versus frequency). In general, a phase angle approaching 90° at low frequency  
32 indicates an ideal capacitive response. Here, the phase angles for SrWO<sub>4</sub>, rGO, and  
33 SrWO<sub>4</sub>/rGO are around -50°, -54°, and -57° in the low-frequency region, implying a mixed



1 response with a pronounced pseudocapacitive/redox contribution rather than a purely electric  
2 double-layer capacitor. Overall, these EIS results support that the redox-active character of the  
3 electrode, enhanced by the SrWO<sub>4</sub>/rGO synergy, is a key factor enabling high total charge  
4 storage. Another parameter is the relaxation time constant  $\tau_0$ , a kinetic parameter obtained from  
5 EIS analysis, specifically from the Bode plot (**Fig. S6**). It clearly explains the minimum time  
6 required for a SC electrode to deliver more than 50% of its stored energy with an efficiency  
7 greater than 50%.

8  $\tau_0 = 1 / f_0(4)$  where  $f_0$  is the characteristic  
9 frequency at which the Bode plot's phase angle equals  $-45^\circ$ , or the precise point where the  
10 capacitive and resistive impedances match.<sup>63</sup> The  $\tau_0$  and  $f_0$  value for SrWO<sub>4</sub>, rGO, SrWO<sub>4</sub>/rGO  
11 are 5.88 (s), 2.22 (s), 0.86 (s) and 0.17 (Hz), 0.45 (Hz), 1.16 (Hz). The enhanced performance  
12 is attributed to the rGO sheets incorporated with SrWO<sub>4</sub> particles, which provide a large surface  
13 area and porous structure that facilitates rapid electron and ion transport.<sup>32</sup> The SrWO<sub>4</sub> and  
14 SrWO<sub>4</sub>/rGO electrode component's Faradaic activity is reflected in the GCD curves (**Fig. 6.**  
15 **(c-d)**), which exhibit battery-like behaviour at the full current density. At higher charge and  
16 discharge rates, this phenomenon is ascribed to restrictions in electrolyte ion mobility.<sup>4</sup>  
17 Nonetheless, SrWO<sub>4</sub>/rGO electrode (**Fig. 8. (b)**) clearly illustrates the trade-off between specific  
18 capacitance of approximately 727, 478, 357, 279 and 168  $F g^{-1}$  at 1, 3, 6, 8, and 10  $A g^{-1}$ ,  
19 respectively. At higher current densities, limited ion diffusion within the electrode material  
20 results in incomplete Faradaic reactions at the electrode surface. As a result, when the current  
21 density increases, the charge/discharge time decreases. The battery-like features of the GCD  
22 curves show the Faradaic behaviours of the electrode's (SrWO<sub>4</sub>/rGO) components over the  
23 whole current density range. The  $C_s$  values for SrWO<sub>4</sub>, rGO and SrWO<sub>4</sub>/rGO at different  
24 discharge current densities are shown in **Fig. 8. (b)** in a 1 M KOH electrolyte based on the  
25 above-mentioned equation. The cooperative relationship between rGO and SrWO<sub>4</sub>, which  
26 increases the number of active sites for Faradaic reactions and improves the charge transfer  
27 kinetics, is responsible for this improved performance (SrWO<sub>4</sub>/rGO). As a result, only a portion  
28 of the active surface participates in charge storage, thereby reducing the specific capacitance.<sup>64</sup>  
29 When using SC in practical applications, long-term cyclic stability is another critical factor to  
30 consider. As presented in **Fig. 8. (c)**, after 5000 cycles at a current density of 10  $A g^{-1}$ , the  
31 SrWO<sub>4</sub>/rGO electrode retained 95 % of its initial capacitance. It also exhibited an outstanding  
32 Coulombic efficiency of 96.5 %. These results indicate that the electrode material maintained



1 excellent stability throughout the cycling process. The first and last ten cycles from the cycling  
2 stability test are shown in the inset of **Fig. 8. (c)**. Post-cycling XRD (**Fig. 10. (a-b)**) and SEM  
3 (**Fig. 11**) analyses both tend to confirm the stability of the material's post-cycles. Pre and Post  
4 cyclic stability XRD for SrWO<sub>4</sub> and SrWO<sub>4</sub>/rGO as shown in **Fig.S3. (a-b)**. Post-cycling XRD  
5 pattern has retained all the crystalline peaks of the material compared to the Pre-cycling XRD  
6 pattern; however, there is a considerable decline in intensity due to lattice distortion caused by  
7 expansion/contraction during electrochemical absorption/desorption. Post-cyclic SEM  
8 micrographs. The synthesised SrWO<sub>4</sub>/rGO electrode exhibits a remarkably high specific  
9 capacity in 1 M KOH electrolyte, surpassing that of previously reported metal tungstate-based  
10 SC electrodes (**Table S3**).

11

### 12 **3.4 Electrochemical Characteristics of the Solid-State Symmetric Supercapacitor:**

13 To further evaluate its practical potential, a solid-state symmetrical two-electrode SCs (STS)  
14 was constructed using SrWO<sub>4</sub>/rGO as both electrodes (positive and negative). The electrolyte  
15 was a 1 M PVA-KOH gel, operating within 0 – 2.0 V. **Fig. 9. (a)** demonstrates the CV studies  
16 of the STS at various scan rates (10 – 100 mV s<sup>-1</sup>). Each CV curve exhibits Faradaic  
17 behaviour and remains consistent across all current densities. Moreover, the current density  
18 consistently increases with the scan rate, rising from 10 – 100 mV s<sup>-1</sup>, demonstrating the STS  
19 material's excellent rate capability. Likewise, **Fig. 9. (b)** displays the GCD test outcomes  
20 within 0 – 1.5 V at 1 to 10 A g<sup>-1</sup>. The GCD curves further demonstrate the device's high-  
21 power capability by exhibiting characteristic pseudocapacitive behaviour, as evidenced by a  
22 nonlinear shape and minimal IR drop across this wide potential range. **Fig. 9. (c)** presents the  
23 Nyquist plot of the fabricated device, with the slope indicating the ion adsorption rate within  
24 the electrode material. A steeper slope approaching the y-axis signifies a higher adsorption rate  
25 or improved capacitive performance of the active material. The EIS parameters in the two-  
26 electrode symmetric device configuration show the anticipated increase: R<sub>s</sub> = 1.3 Ω and R<sub>ct</sub> =  
27 4.2 Ω. This is consistent with reports for similar symmetric SC devices, where two-electrode  
28 R<sub>s</sub> and R<sub>ct</sub> values are higher than those for three-electrode devices.<sup>10</sup> Extracted from the two-  
29 electrode Bode phase plot, the device-level relaxation time constant (2E) τ<sub>0</sub> = 1.18 s (f<sub>0</sub> = 0.85  
30 Hz) is competitive with similar tungstate-based composite devices, indicating that the practical  
31 device maintains the fast kinetic advantages imparted by the rGO scaffold. The superior  
32 charge-transport characteristics of the STS for high-performance SC applications are



1 confirmed by a systematic comparison of EIS parameters between the two configurations,  
 2 which provides a comprehensive kinetic picture that separates the intrinsic material response  
 3 (three electrodes) from the practical device performance. These characteristics indicate that the  
 4 STS electrode is well-suited for high-performance SC applications. As shown in **Fig. 9. (d)**,  
 5 the following measurements corresponding to **Fig. 9. (b)** were conducted at discharge current  
 6 densities of 1, 3, 6, 8, and 10  $A g^{-1}$ , the specific capacitances of the STS were found to be  
 7 83.6, 53.9, 38.5, 20.3, and 13  $F g^{-1}$ , respectively. This decrease is due to poor ion insertion  
 8 behaviour, which reduces specific capacitance. The energy density ( $E$ ) and power density ( $P$ )  
 9 of the STS device were calculated using the following Eq. (5-6):<sup>65</sup>

$$10 \quad E = \frac{C_s \Delta v^2}{7.2} (Wh kg^{-1}) \quad (5)$$

$$11 \quad P = E/\Delta t (W kg^{-1}) \quad (6)$$

12 where  $\Delta t$  is the discharge time (s),  $\Delta V$  is the cell operating voltage window, and  $C_s$  denotes the  
 13 specific capacitance ( $F g^{-1}$ ) of the STS, determined using the total mass of the active materials.  
 14 **Fig. 9. (e)** presents the Ragone plot of the STS device. The device exhibited a power density  
 15 of 2159.5  $W kg^{-1}$  at an energy density of 26.13  $Wh kg^{-1}$ , and maintained a stable power  
 16 density of 3.5  $W kg^{-1}$  with an energy density of 132.8  $Wh kg^{-1}$  at 10  $A g^{-1}$ . For practical  
 17 STS applications, long-term cycling stability is a key metric. To evaluate the cycling behaviour  
 18 of the STS electrode, GCD profiles from the first and last five cycles were compared, as shown  
 19 in the inset of **Fig. 9. (f)**. The STS electrode exhibited remarkable capacity retention of 96.2%  
 20 and a high Coulombic efficiency of 98.4%, as shown in **Fig. 9. (f)**. Despite some performance  
 21 degradation due to significant volume changes during charge-discharge cycling, which affected  
 22 the reversibility of the redox reactions, the SrWO<sub>4</sub>/rGO nanocomposite showed excellent  
 23 overall stability.<sup>66</sup> To analyze the Post-cyclic stability of materials, XRD and SEM were  
 24 performed. The post-cycling XRD pattern shows retention of all crystalline peaks of the  
 25 material compared to the pre-cycling pattern (**Fig. 10**); however, a considerable decline in  
 26 intensity is observed due to lattice distortion caused by expansion/contraction during  
 27 electrochemical absorption/desorption. As shown in **Fig. 11**, HR-SEM images of the  
 28 SrWO<sub>4</sub>/rGO electrode after 5000 cycles reveal no significant morphological changes,  
 29 indicating excellent structural stability. The electrode components were recovered via  
 30 ultrasonic dispersion in deionised (DI) water after the stability test. Minor, fragmented, and  
 31 finer features observed in some regions may result from enhanced adhesion between the active



1 material and the nickel foam (NF), facilitated by the PVDF binder. This improved interfacial  
2 adhesion likely contributes to the device's superior long-term cycling stability.<sup>4</sup>

### 3 **4. Conclusion**

4 In summary, SrWO<sub>4</sub>/rGO was successfully synthesised via a facile one-pot  
5 hydrothermal approach, and the resulting nanocomposite was verified using various  
6 spectroscopic and analytical techniques. The as-synthesized SrWO<sub>4</sub>/rGO electrode exhibited  
7 superior performance compared to bare SrWO<sub>4</sub>. At the same time, the porous rGO enhances  
8 interfacial contact and increases the number of active sites, thereby augmenting electrolyte  
9 interaction. The three-electrode test demonstrated that the SrWO<sub>4</sub>/rGO electrode achieved an  
10 excellent specific capacitance of 727 F g<sup>-1</sup> at 1 A g<sup>-1</sup>, and 95 % retention after 5000 cycles  
11 at 10 A g<sup>-1</sup>. The high capacitance results from the strategic synergy between rGO's electrical  
12 double-layer capacitance and SrWO<sub>4</sub>'s pseudocapacitive behaviour. Based on this, the  
13 synthesised SrWO<sub>4</sub>/rGO was used as both the positive and negative electrodes to form an STS  
14 supercapacitor. The resulting STS device delivered an outstanding specific capacitance of  
15 83.6 F g<sup>-1</sup>, energy density of 26.13 Wh kg<sup>-1</sup> and the power density of 2159.5 W kg<sup>-1</sup>. The  
16 STS system demonstrated exceptional long-term cycling stability, enduring over 5000 cycles,  
17 alongside impressive high-rate capability (96.2% retention at 10 A g<sup>-1</sup>). The SrWO<sub>4</sub>/rGO SC  
18 electrode demonstrates significant potential for next-generation energy storage applications,  
19 and this study expands the prospects for developing advanced energy storage devices. Future  
20 work should systematically examine the effect of SrWO<sub>4</sub> on GO incorporation ratios on the  
21 electrochemical behaviour of the hybrid material to enhance capacitive performance further  
22 and advance SC applications.



**1 Associate Content****2 Supporting Information**

**3 Fig. S1.** UV-vis spectra for rGO (black curve), SrWO<sub>4</sub> (red curve) and SrWO<sub>4</sub>/rGO (blue curve).

**4 Fig. S2. (a)** CV curves at 50 mV s<sup>-1</sup> and GCD curves at 1 A g<sup>-1</sup> for SrWO<sub>4</sub> (red curve) and  
**5** SrWO<sub>4</sub>/rGO (blue curve) in 1 M KOH electrolyte.

**6 Fig. S3.** XRD of SrWO<sub>4</sub> **(a)** and SrWO<sub>4</sub>/rGO **(b)** Pre and Post cyclic stability.

**7 Fig. S4. (a)** CV of SrWO<sub>4</sub> at 50 mV s<sup>-1</sup>, **(b)** Logarithmic relationship of scan rate vs peak  
**8** current density, **(c)** Capacitance contribution of SrWO<sub>4</sub> at 10 – 100 mV s<sup>-1</sup> **(d)** The square  
**9** root of the scan rate is shown against the peak current density.

**10 Fig. S5. (a-b)** W-H plot for SrWO<sub>4</sub> and SrWO<sub>4</sub>/rGO, **(c-d)** Bode phase and Bode plot for  
**11** SrWO<sub>4</sub>, rGO, SrWO<sub>4</sub>/rGO.

**12 Fig. S6. (a-b)** Bode phase and Bode plot for SrWO<sub>4</sub>/rGO-SSC.

**13 Table S1.** - Crystalline parameters of the prepared materials.

**14 Table S2.** Electrochemical Impedance Parameters.

**15 Table S3.** -Electrochemical performance comparison of metal tungstate-based SCs electrodes.

**16 Author's Information****17 Corresponding Author**

**18 Prof. Dr. Arockia Selvi J**

**19** Department of Chemistry, SRM Institute of Science and Technology, Kattankulathur – 603203,  
**20** Tamil Nadu, India.

**21** Email: [arockiaj@srmist.edu.in](mailto:arockiaj@srmist.edu.in)

**22** ORCID ID: 0000-0003-4505-4064

**23**

**24 Authors**

**25 Sabarikaruthapandi Ramar**

**26** Department of Chemistry, SRM Institute of Science and Technology, Kattankulathur – 603203,  
**27** Tamil Nadu, India.

**28** Email: [sr9651@srmist.edu.in](mailto:sr9651@srmist.edu.in)

**29** ORCID ID: 0009-0001-9722-3010



**Dr. Ponnaiah Sathish Kumar**

Department of Chemical Engineering, Pohang University of Science and Technology (POSTECH), Pohang 37673, Republic of Korea.

Email: [skponnaiah@postech.ac.kr](mailto:skponnaiah@postech.ac.kr)

ORCID ID: 0000-0002-5572-7683

**Bharathi Kannan Raja**

Department of Chemistry, SRM Institute of Science and Technology, Kattankulathur – 603203, Tamil Nadu, India.

Email: [br4149@srmist.edu.in](mailto:br4149@srmist.edu.in)

ORCID ID: 0000-0002-2643-2501

**Dr. Muthukumar Govindaraj**

Department of Chemistry, SRM Institute of Science and Technology, Kattankulathur – 603203, Tamil Nadu, India.

Institute of Industrial Science, The University of Tokyo, 4-6-1 Komaba, Meguro-Ku, Tokyo 153–8505, Japan.

Email: [gmkumar2712@gmail.com](mailto:gmkumar2712@gmail.com), [gmkumar@iis.u-tokyo.ac.jp](mailto:gmkumar@iis.u-tokyo.ac.jp)

ORCID ID: 0000-0001-6034-564X

**Acknowledgments**

We acknowledge the SCIF and the Nanotechnology Research Centre (NRC) at SRMIST and the Department of Chemistry for providing research facilities.

**Declaration of Competing Interest**

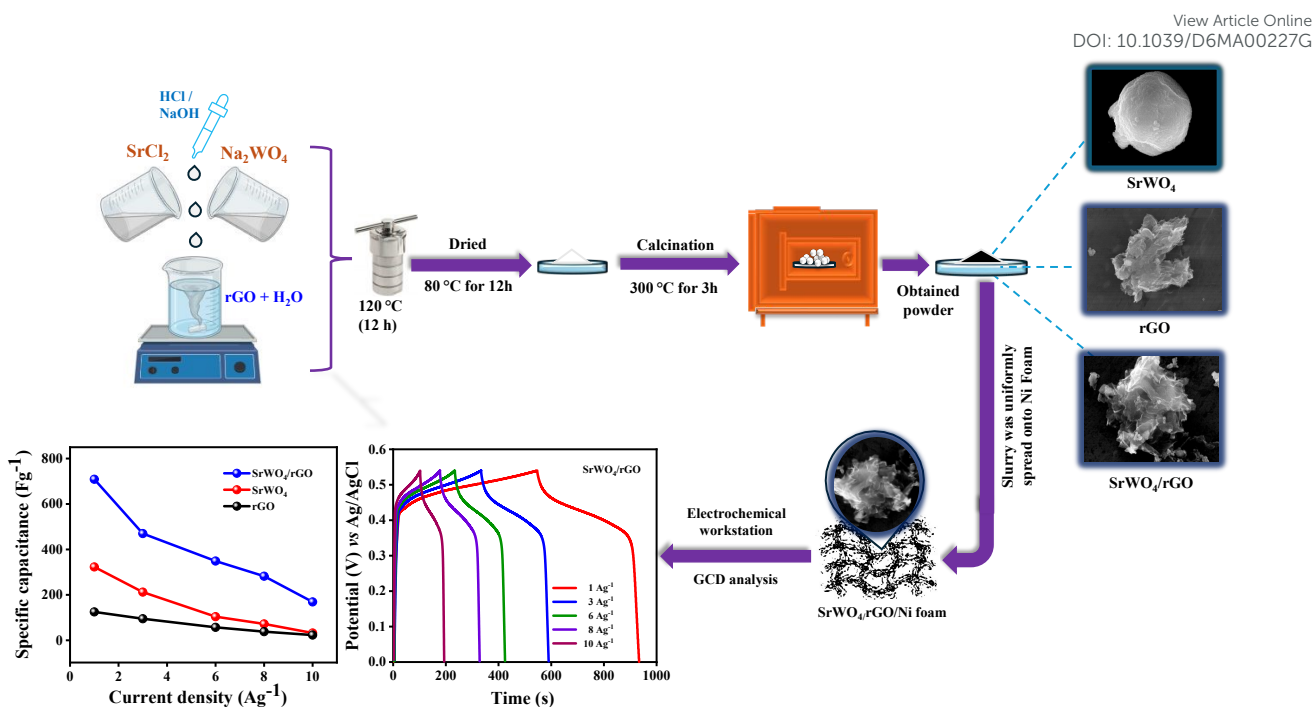
The authors declare that they have no known competing financial interests or personal relationships that could have appeared to influence the work reported in this paper.

**Author Contributions**

**S.R:** Conceptualization, formal analysis, experimental operation, validation, data curation, writing original draft, review and editing; **P.S:** Validation, visualization, data curation, writing review and editing, revising the manuscript; **B.R & M.G:** Data curation, validation, writing review and editing, revising the manuscript; **J.A.S:** Conceptualization, investigation, visualization, supervision, validation, data curation, project administration, resources, writing review and editing the original manuscript.



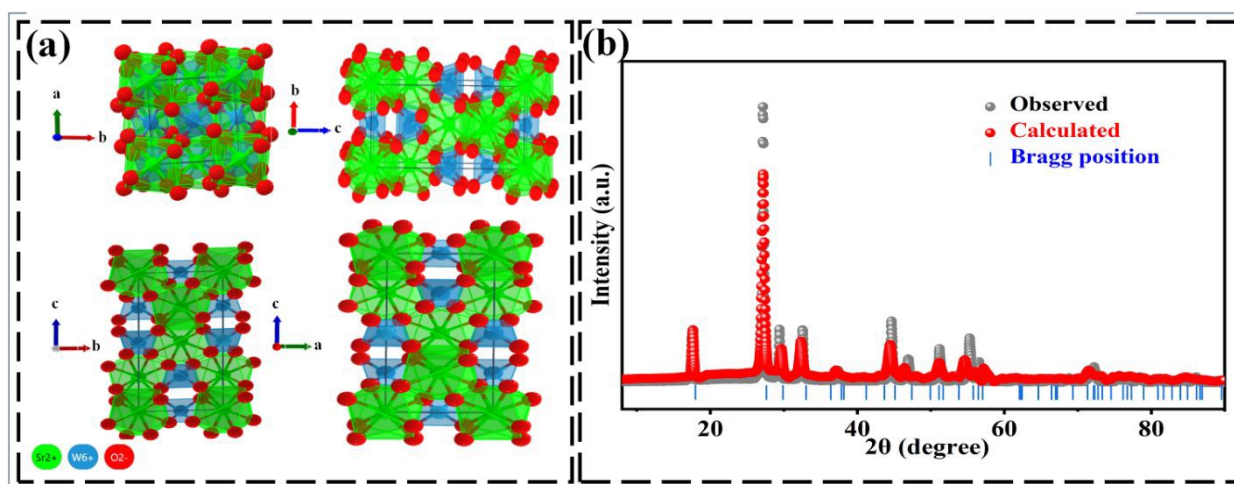
1



2

3 **Scheme 1.** Schematic illustration of the hydrothermal synthesis of SrWO<sub>4</sub>/rGO nanocomposite,  
4 and Electrochemical analysis with GCD and its specific capacitance curves.

5



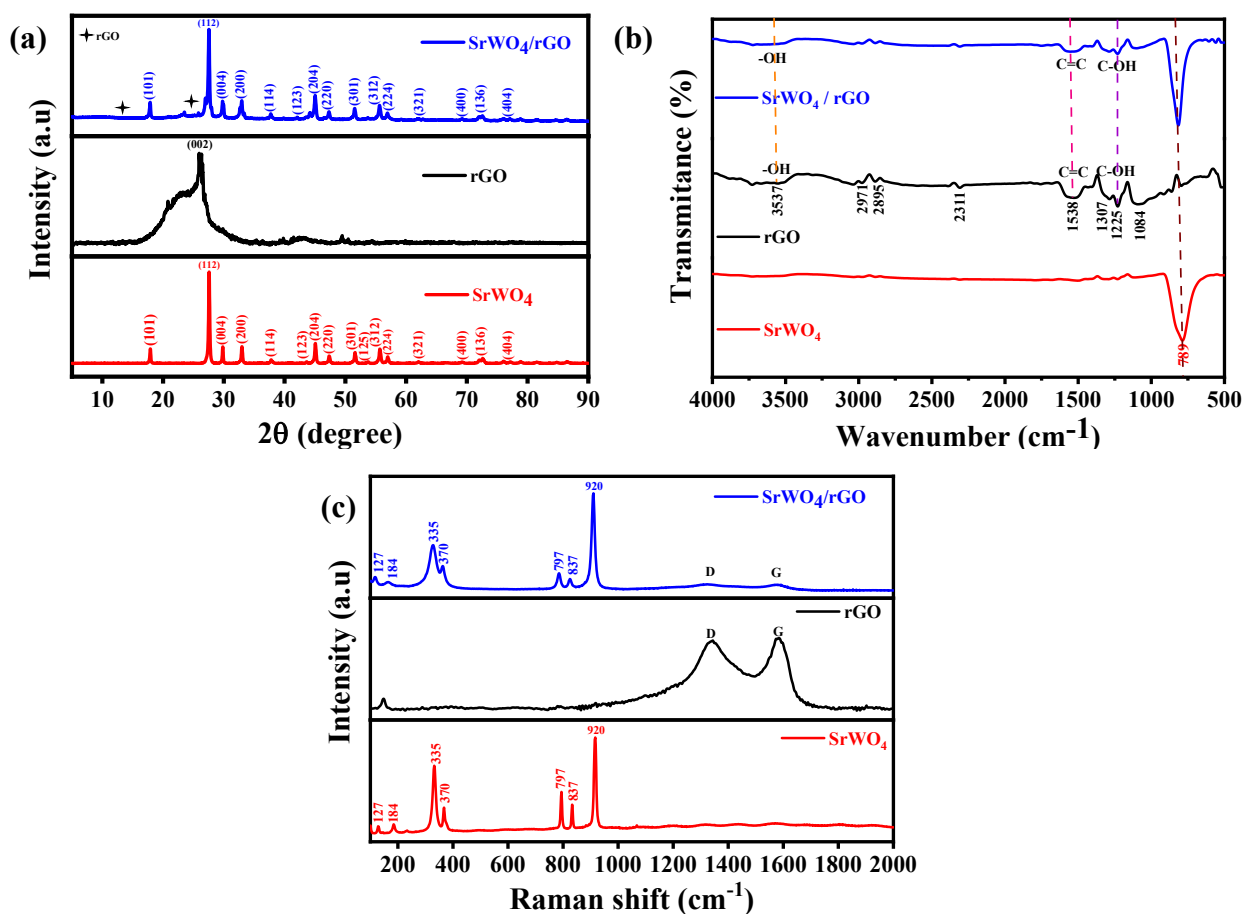
6

7 **Fig. 1** (a) Crystal structure of SrWO<sub>4</sub> in different geometries. (b) Theoretically calculated pattern exhibited minimal deviation from bragg position. Data retrieved from the Materials Project for SrWO<sub>4</sub> (mp-19163) from database version v2025.09.25.

7



1



2

3

4 **Fig. 2** Crystalline characteristics, Phase purity, and Material composition: **(a-c)** X-ray  
 5 diffraction pattern, Stacked comparative FT-IR spectrum, and Raman spectra of SrWO<sub>4</sub>, rGO  
 6 and SrWO<sub>4</sub>/rGO nanocomposite.

7

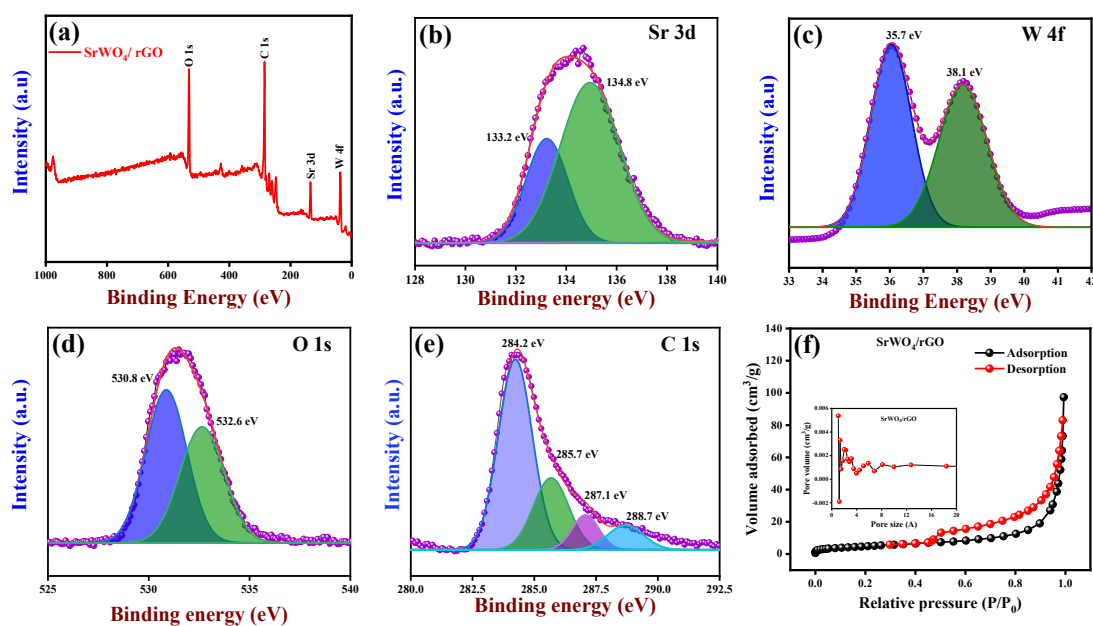
8

9

10



1

View Article Online  
DOI: 10.1039/D6MA00227G

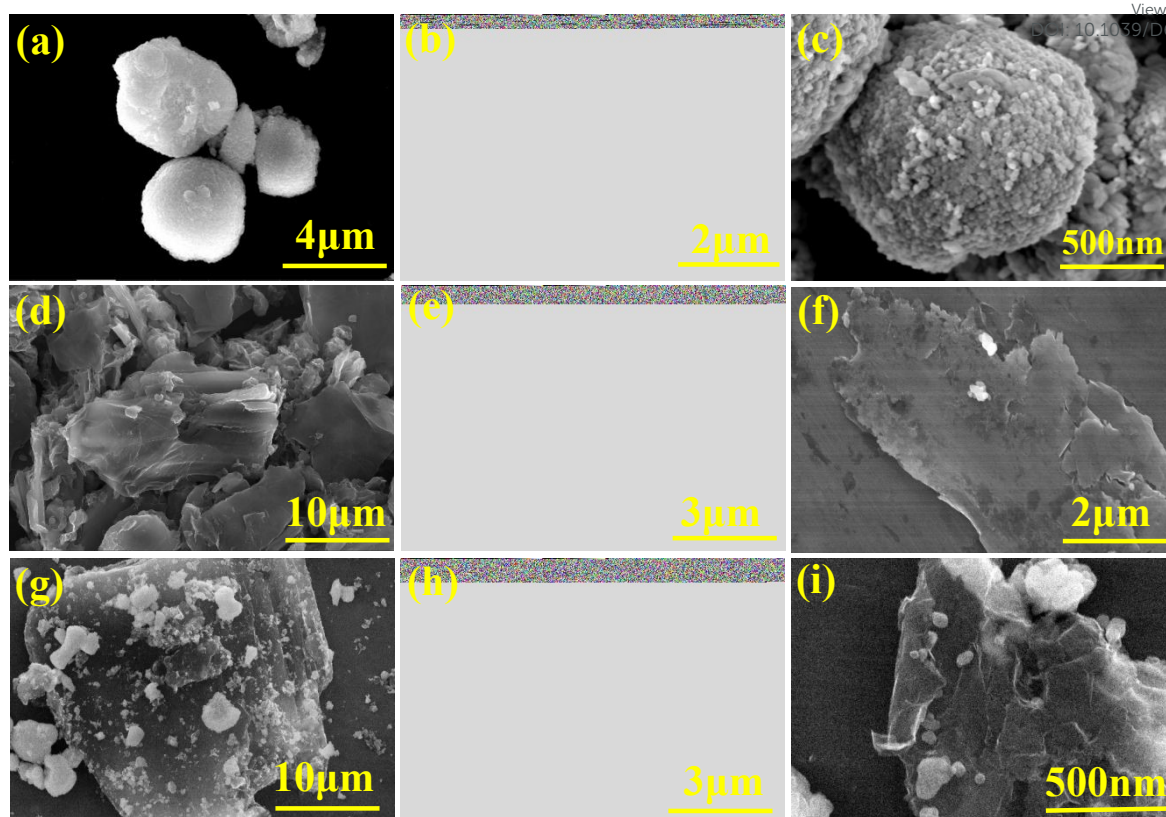
2

3

4

5 **Fig. 3.** Material composition, Surface chemical state, and surface area through X-Ray  
 6 Photoelectron Spectroscopy (XPS) and BET analysis: (a) XPS Survey scan of SrWO<sub>4</sub>/rGO  
 7 nanocomposites. Deconvoluted high-resolution XPS spectrum of (b) Sr 3d confirming the 3d<sub>3/2</sub>  
 8 and 3d<sub>5/2</sub> spin-orbit levels, (c) W 4f confirming tungsten in the W<sup>6+</sup> with W 4f<sub>5/2</sub> and W 4f<sub>7/2</sub>  
 9 spin-orbit levels, (d) O 1s confirming metal oxygen bonds and chemisorbed oxygen  
 10 originating from surface hydroxyl groups, (e) C 1s confirming the presence of aromatic carbon  
 11 species and functional groups, indicating effective GO removal and (f) Nitrogen adsorption and  
 12 desorption isotherm of SrWO<sub>4</sub>/rGO nanocomposites (inset: pore size distribution curve).



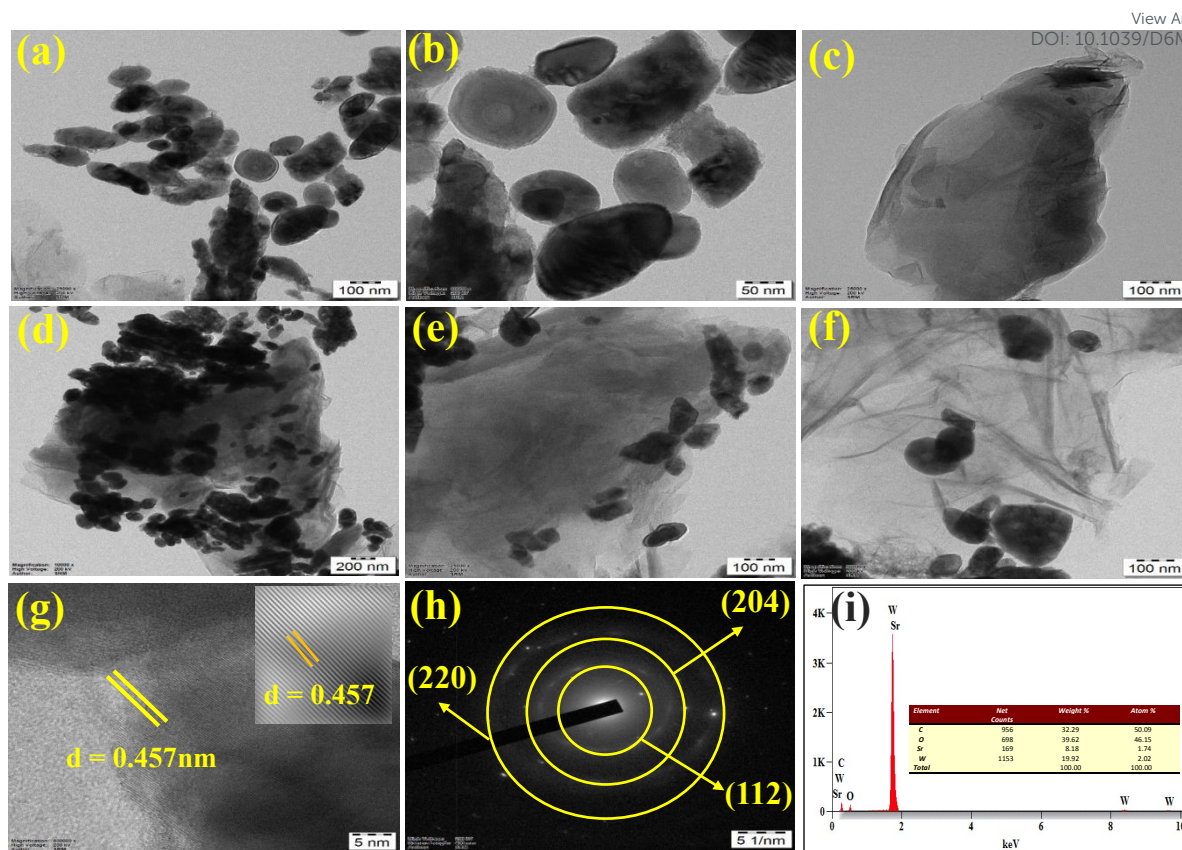


1

2

3 **Fig. 4.** HR-SEM Micrographs of (a-c) SrWO<sub>4</sub>, (d-f) rGO, and (g-i) SrWO<sub>4</sub>/rGO  
4 Nanocomposite.





1  
2  
3  
4  
5  
6

**Fig. 5.** HR-TEM Micrographs of (a-b)  $\text{SrWO}_4$ , (c) rGO, (d-f)  $\text{SrWO}_4/\text{rGO}$  nanocomposites, (g) Lattice fringes of  $\text{SrWO}_4$ , (h-i) SAED pattern and EDX spectrum of  $\text{SrWO}_4/\text{rGO}$  nanocomposites, with inset (i) table showing the weight and atomic percentages of detected elements.



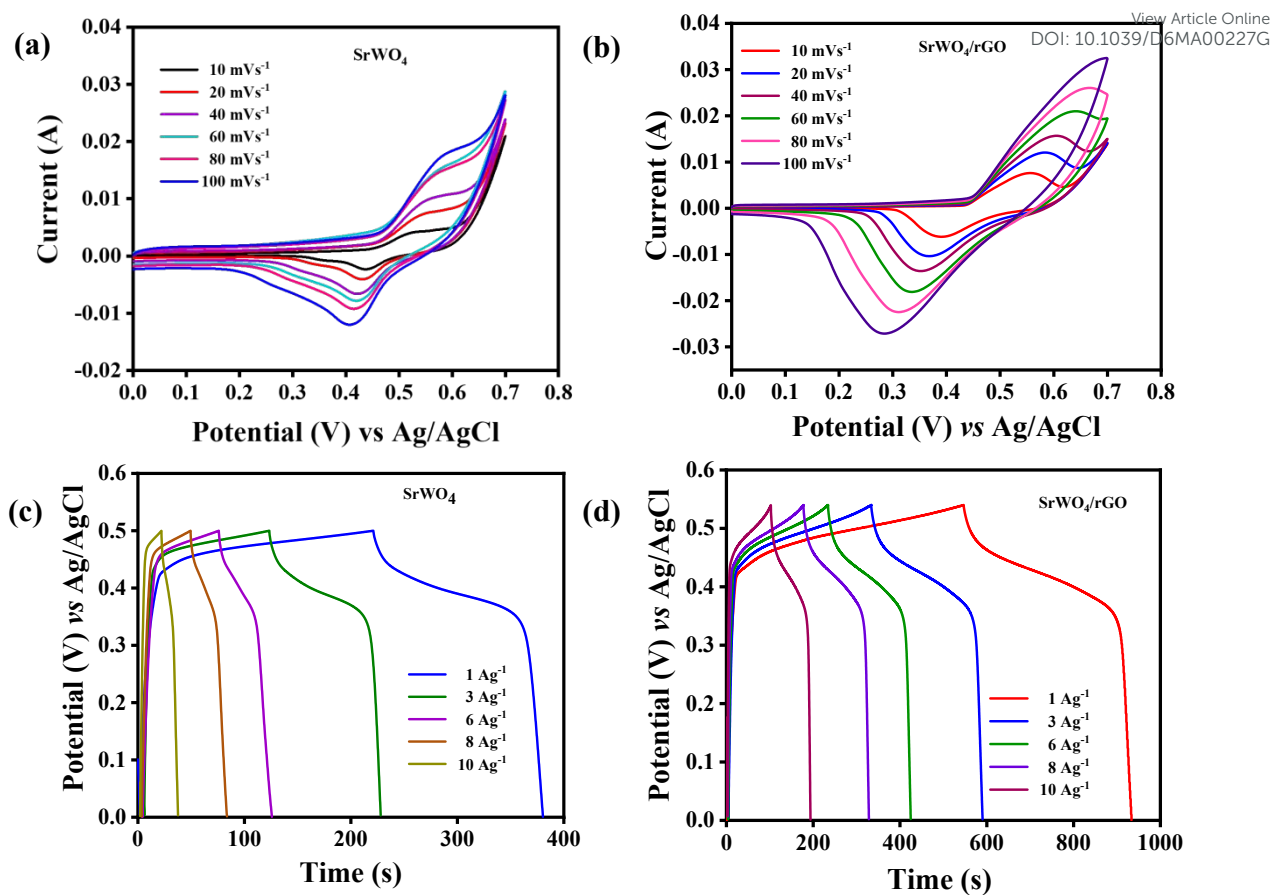


**Fig. 6.** Electrochemical redox behaviour through CV-curves at scan rate of 10 to 100  $mV s^{-1}$  for (a) SrWO<sub>4</sub>, and (b) SrWO<sub>4</sub>/rGO and GCD curves at 1 to 10  $A g^{-1}$  for (c) SrWO<sub>4</sub>, and (d) SrWO<sub>4</sub>/rGO in 1 M KOH electrolyte.

1  
2  
3  
4  
5  
6  
7



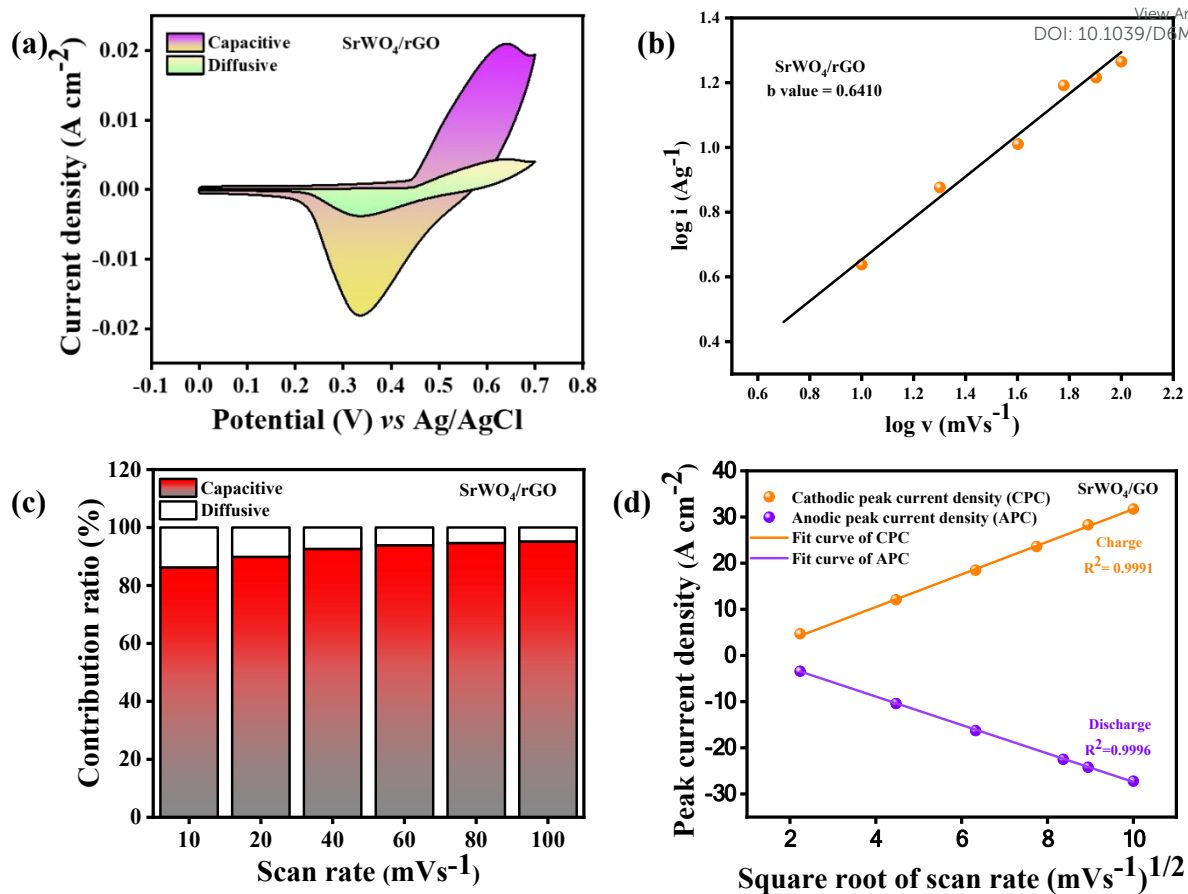


**Fig. 7.** Dunn method calculation of (a) CV of SrWO<sub>4</sub>/rGO at 50 mVs<sup>-1</sup>, (b) Logarithmic relationship of scan rate vs peak current density, (c) capacitance contribution of SrWO<sub>4</sub>/rGO at 10 -100 mV s<sup>-1</sup>, (d) The square root of the scan rate shown against the peak current density.

1  
2  
3



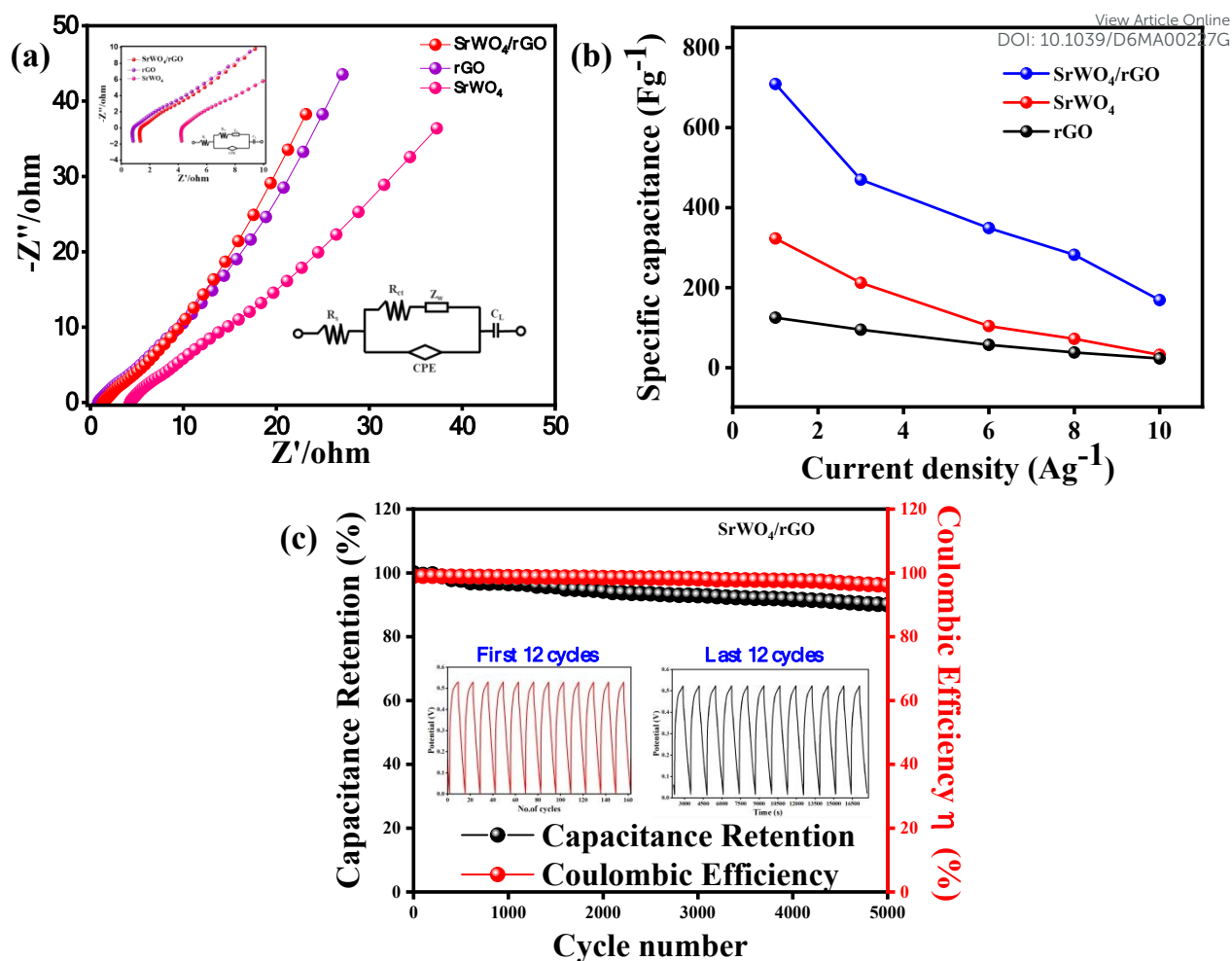


**Fig. 8.** (a) Interfacial impedance characteristics simulated through Nyquist plots of SrWO<sub>4</sub>, rGO, and SrWO<sub>4</sub>/rGO nanocomposite (inset: Zoomed-in image of the high-frequency region.) (b) Specific capacitance quantification curves of the various SrWO<sub>4</sub> and SrWO<sub>4</sub>/rGO composites at different current densities 1 – 10 A g<sup>-1</sup>, and (c) Cyclic stability of SrWO<sub>4</sub>/rGO at 10 A g<sup>-1</sup> in a three-electrode system (inset: first 12 and last 12 cycles).

1

2

3

4

5

6

7

8

9

10



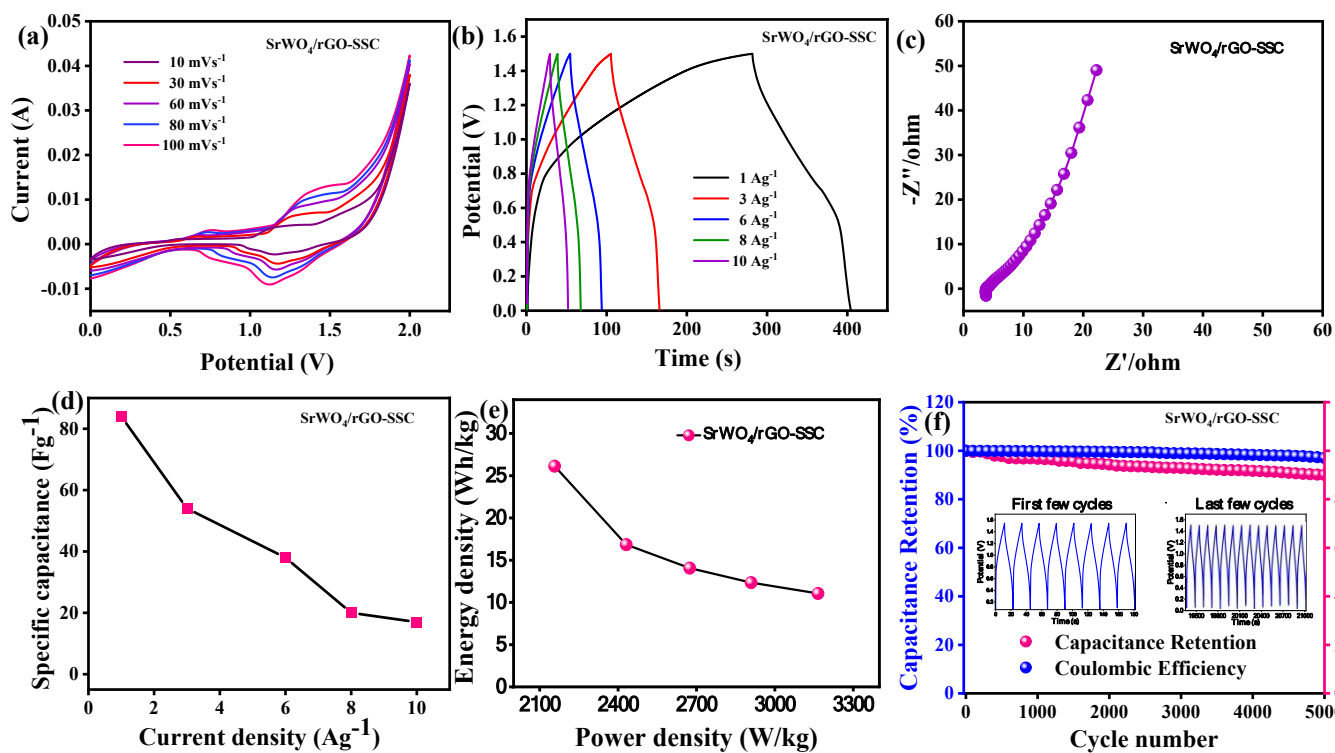


**Fig. 9.** (a) CV (b) GCD curves, and (c) EIS spectra for the STS device of SrWO<sub>4</sub>/rGO//SrWO<sub>4</sub>/rGO. (d) Specific capacitances of the STS at 1.0 to 10 A g<sup>-1</sup>. (e) Ragone plot of the STS. (f) Coulombic efficiency and Capacitance retention vs the number of cycles for STS (inset: first and last few cycles).



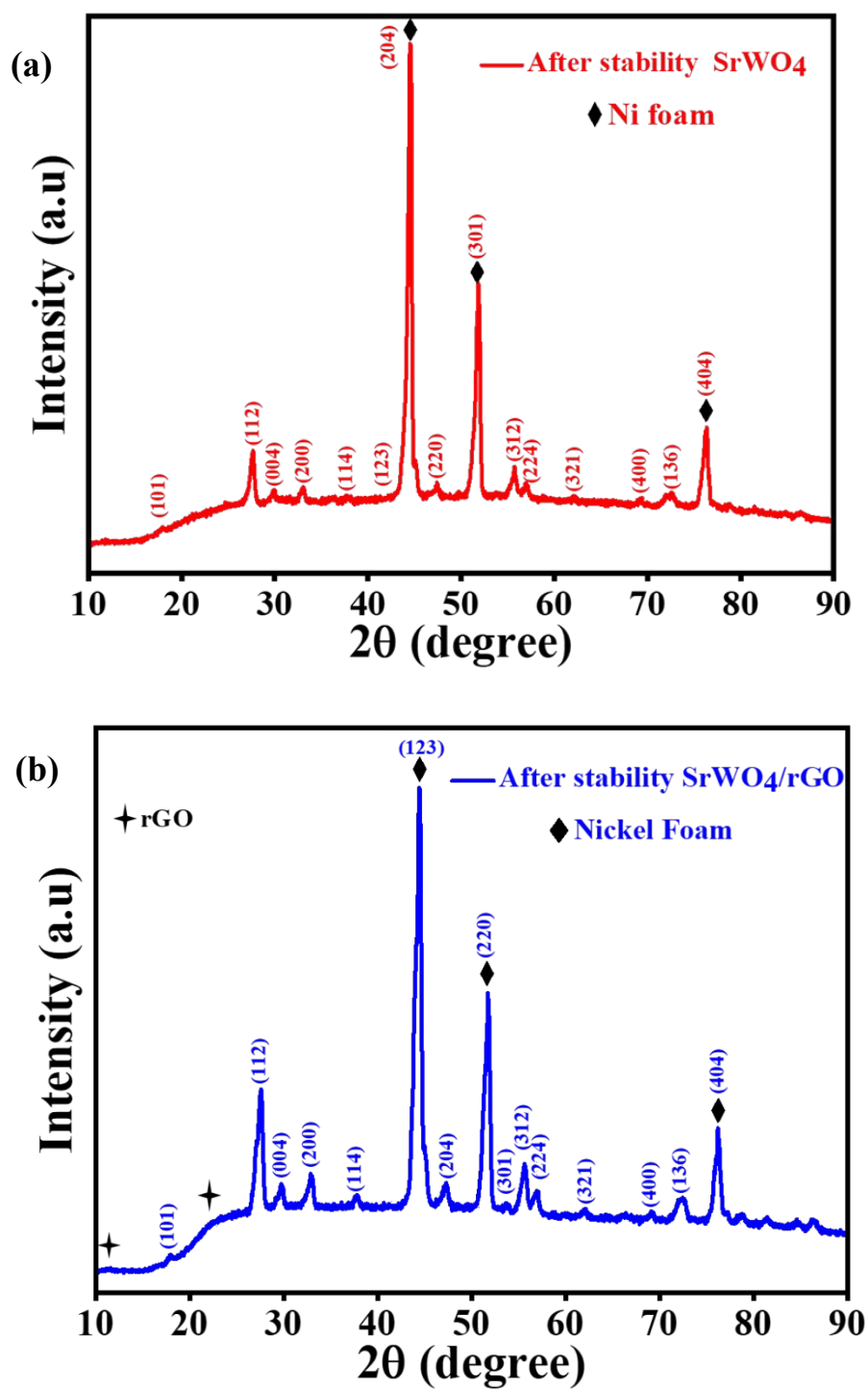
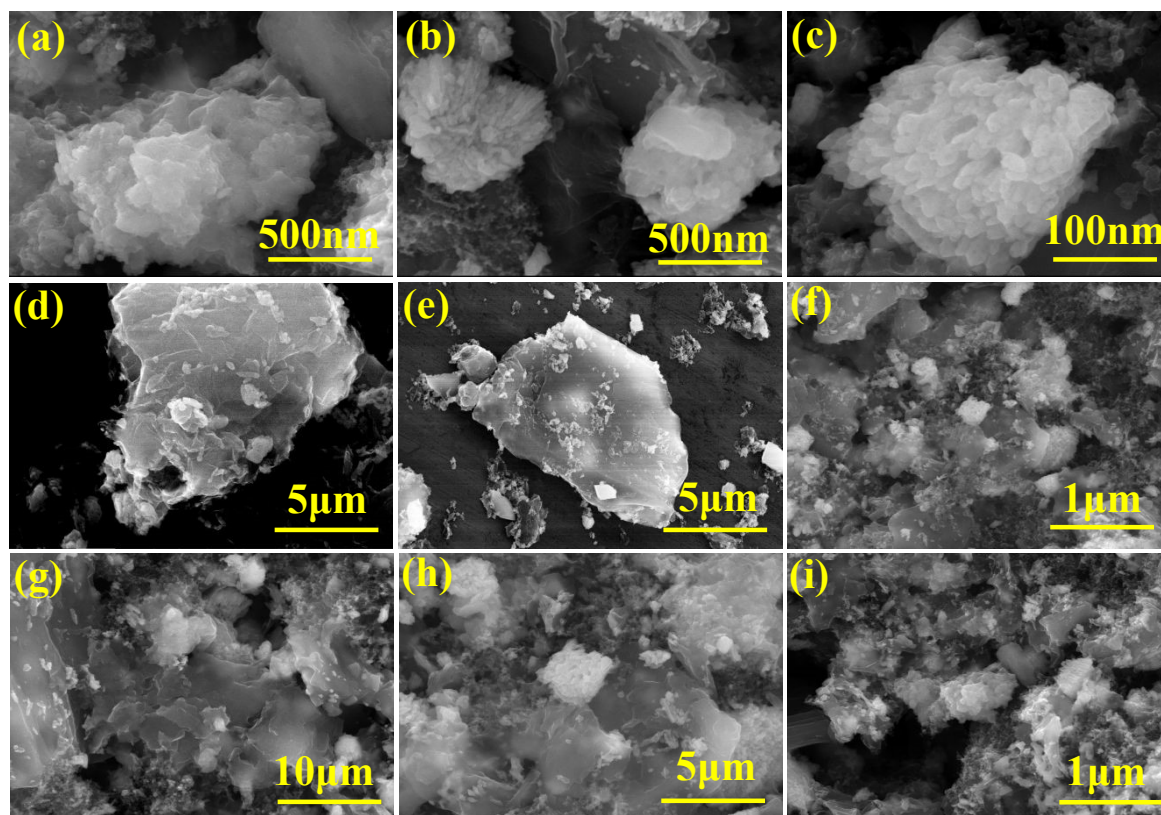


Fig. 10. Post cyclic stability XRD for SrWO<sub>4</sub> (a) and SrWO<sub>4</sub>/rGO nanocomposite (b)





**Fig. 11.** Post HR-SEM Micrographs of (a-c) SrWO<sub>4</sub>, (d-e) rGO, and (f-i) SrWO<sub>4</sub>/rGO Nanocomposite



1 **References**

- 2 1. B. Muthukutty, P. Sathish Kumar, D. Lee and S. Lee, *ACS nano*, 2024, **18**, 27287–  
3 27316.
- 4 2. S. Ramar, P. Sathish Kumar, M. Govindaraj, M. K. Muthukumaran and B. K. Raja,  
5 *Energy & Fuels*, 2025, **39**, 10070–10082.
- 6 3. M. Karthikeyan, S. Rajkumar and M. Priyadharshan, *Journal of Industrial and*  
7 *Engineering Chemistry*, 2025, **147**, 608–618.
- 8 4. P. S. Kumar, J. Bae, J. W. Roh, Y. Min and S. Lee, *Nano convergence*, 2025, **12**, 21.
- 9 5. S.-K. Kim, H. J. Kim, J.-C. Lee, P. V. Braun and H. S. Park, *ACS nano*, 2015, **9**, 8569–  
10 8577.
- 11 6. S. Rajkumar and J. Qin, in *Supercapacitors: Fundamentals, Advances and Future*  
12 *Applications*, eds. D. K. Verma and J. Aslam, Royal Society of Chemistry, 2025, vol.  
13 3, p. 0.
- 14 7. P. S. Kumar, Y. Min, D. C. Hyun, J.-H. Choi and S. Lee, *Journal of Energy Storage*,  
15 2023, **74**, 109385.
- 16 8. R. P. Dhavale, V. G. Parale, A. M. Teli, N. K. Gupta, U. M. Patil, H. Choi, A. M. Patil,  
17 V. D. Phadtare, A. A. Ransing and H.-H. Park, *ACS Applied Materials & Interfaces*,  
18 2025, **17**, 25193–25205.
- 19 9. M. Ganesan, S. Alagar, S. M. Jeong and S. Piraman, *ACS Applied Nano Materials*,  
20 2025, **8**, 14531–14546.
- 21 10. S. Rajkumar, S. Dhineshkumar, N. Arunprakash, P. Raychel and J. P. Merlin, *Optical*  
22 *Materials*, 2023, **142**, 113934.
- 23 11. M. D. Angelin, S. Rajkumar, A. Ravichandran, M. M. Alam and A. G. Al-Sehemi,  
24 *Journal of Industrial and Engineering Chemistry*, 2025, **147**, 436–447.
- 25 12. S. Rajkumar and J. Qin, *Journal of Water Process Engineering*, 2025, **79**, 108920.
- 26 13. D. Panda, S. Hota, L. Biswal and R. P. Choudhary, *Transactions on Electrical and*  
27 *Electronic Materials*, 2025, **26**, 380–394.
- 28 14. S. S. Hota, D. Panda, S. Bhoobash, L. Biswal, S. Mishra and R. N. P. Choudhary,  
29 *Polymer Bulletin*, 2025, **82**, 7319–7342.
- 30 15. S. S. Hota, D. Panda, L. Biswal and R. N. P. Choudhary, *Journal of Electronic*  
31 *Materials*, 2024, **53**, 4018–4029.
- 32 16. S. S. Hota, D. Panda and R. Choudhary, *Journal of the Korean Ceramic Society*, 2024,  
33 **61**, 1207–1221.



- 1 17. D. Panda, S. S. Hota and R. Choudhary, *Journal of Solid State Chemistry*, 2024, **331**,  
2 124531. View Article Online  
DOI: 10.1039/D4MA00227G
- 3 18. D. Panda, S. S. Hota and R. Choudhary, *Inorganic Chemistry Communications*, 2023,  
4 **158**, 111501.
- 5 19. B. Muthukutty, A. Krishnapandi and S.-M. Chen, *New Journal of Chemistry*, 2020, **44**,  
6 2489–2499.
- 7 20. M. Govindaraj, J. Rajendran, U. G. P K, M. K. Muthukumaran, B. Jayaraman and A.  
8 S. J, *ACS Applied Nano Materials*, 2023, **6**, 930–945.
- 9 21. B. Sriram, M. Govindaraj, S.-F. Wang, S. Kogularasu and J. Arockia Selvi, *Chemical*  
10 *Engineering Journal*, 2025, **519**, 165397.
- 11 22. T. Kokulnathan, E. A. Kumar, T.-J. Wang and I.-C. Cheng, *Ecotoxicology and*  
12 *Environmental Safety*, 2021, **208**, 111516.
- 13 23. R. Karthik, P. M. Shafi, S.-M. Chen, R. Sukanya, G. Dhakal and J.-J. Shim, *Journal of*  
14 *the Taiwan Institute of Chemical Engineers*, 2021, **126**, 145–153.
- 15 24. D. Sivaganesh, S. Saravanakumar, V. Sivakumar, S. Sasikumar, J. Nandha Gopal, S.  
16 Kalpana and R. Rajajeyaganthan, *Journal of Materials Science: Materials in*  
17 *Electronics*, 2020, **31**, 8865–8883.
- 18 25. J. Rendón-Angeles, Z. Matamoros-Veloza, L. Gonzalez, J. López-Cuevas, T. Ueda, K.  
19 Yanagisawa, I. Hernández-Calderón and M. Garcia-Rocha, *Advanced Powder*  
20 *Technology*, 2017, **28**, 629–640.
- 21 26. E. Elanthamilan, S. Rajkumar, S. F. Wang and J. P. Merlin, *International Journal of*  
22 *Energy Research*, 2022, **46**, 17113–17125.
- 23 27. A. Bazan-Aguilar, M. Ponce-Vargas, C. L. Caycho, A. La Rosa-Toro and A. M. Baena-  
24 Moncada, *ACS omega*, 2020, **5**, 32149–32159.
- 25 28. S. S. R. Shanlee, M. Govindaraj, T.-W. Chen, S. ming-chen, A. S. J, P. C. R. Stella, S.  
26 S. Taha, M. F. Elsadek and M. S. E, *Process Safety and Environmental Protection*,  
27 2026, **210**, 108663.
- 28 29. B. Chandran, S. Ramasamy, S. K. Ponnaiah, E. Arumugam, S. Chandrasekaran, S.  
29 Karuppaiah and A. Ganesan, *ACS Applied Nano Materials*, 2024, **7**, 6839–6850.
- 30 30. C. Bhuvaneswari, A. Elangovan, C. Sharmila, K. Sudha and G. Arivazhagan, *Colloids*  
31 *and Surfaces A: Physicochemical and Engineering Aspects*, 2023, **656**, 130299.
- 32 31. S. K. Ponnaiah, P. Prakash and B. Vellaichamy, *Ultrasonics Sonochemistry*, 2018, **44**,  
33 196–203.



- 1 32. J. Tang, J. Shen, N. Li and M. Ye, *Journal of Alloys and Compounds*, 2016, **666**, 15–22. View Article Online  
DOI: 10.1039/D6MA00227G
- 2
- 3 33. S. Sultana, M. A. Parvez, N. R. Singha, M. R. Chandan and M. Rahaman, *ACS Applied*
- 4 *Electronic Materials*, 2025, **7**, 8732–8799.
- 5 34. E. Umar, M. W. Iqbal, F. Shaheen, H. Ullah and R. Wahab, *Electrochimica Acta*, 2025,
- 6 **510**, 145339.
- 7 35. H. R. Naderi, A. Sobhani-Nasab, M. Rahimi-Nasrabadi and M. R. Ganjali, *Applied*
- 8 *Surface Science*, 2017, **423**, 1025–1034.
- 9 36. E. Sohoulı, K. Adib, B. Maddah and M. Najafı, *Ceramics International*, 2022, **48**, 295–
- 10 303.
- 11 37. Y. Zhang, L. Li, H. Su, W. Huang and X. Dong, *Journal of Materials Chemistry A*,
- 12 2015, **3**, 43–59.
- 13 38. S. Chinnasamy, J. Madhavan, P. Karthikesan and A. Mani, *Journal of Power Sources*,
- 14 2025, **642**, 236924.
- 15 39. N. K. Ravikumar, N. P. S. Chauhan and P. Perumal, *Dalton Transactions*, 2025, **54**,
- 16 18046–18063.
- 17 40. S. Kaladi Chondath, L. Bansal, B. Sahu and R. Kumar, *ACS Applied Energy Materials*,
- 18 2025, **8**, 8680–8709.
- 19 41. S. S. Hota, D. Panda and R. Choudhary, *Solid State Ionics*, 2023, **399**, 116313.
- 20 42. S. S. Hota, D. Panda and R. Choudhary, *Chinese Journal of Physics*, 2024, **87**, 430–
- 21 451.
- 22 43. X.-r. Li, Y.-h. Jiang, P.-z. Wang, Y. Mo, W.-d. Lai, Z.-j. Li, R.-j. Yu, Y.-t. Du, X.-r.
- 23 Zhang and Y. Chen, *New Carbon Materials*, 2020, **35**, 232–243.
- 24 44. B. RasulKhan, S. K. Ponnaiah, J. Balasubramanian and P. Periakaruppan,
- 25 *Electrocatalysis*, 2022, **13**, 435–446.
- 26 45. X. Liu, Y. Nie, H. Yang, S. Sun, Y. Chen, T. Yang and S. Lin, *Solid State Sciences*,
- 27 2016, **55**, 130–137.
- 28 46. S. Saravanakumar, D. Sivaganesh, V. Sivakumar, S. Sasikumar, T. Thirumalaisamy,
- 29 M. Sayed and A. M. Ali, *Physica Scripta*, 2021, **96**, 125817.
- 30 47. M. K. Muthukumar, M. Govindaraj and A. S. J., *ACS Applied Nano Materials*, 2025,
- 31 **8**, 13381–13393.
- 32 48. G. Bakradze, E. Welter and A. Kuzmin, *Materials*, 2024, **17**, 3071.
- 33 49. N. Dirany, E. McRae and M. Arab, *CrystEngComm*, 2017, **19**, 5008–5021.



- 1 50. X.-M. Yue, Z.-J. Liu, C.-C. Xiao, M. Ye, Z.-P. Ge, C. Peng, Z.-Y. Gu, J.-S. Zhu and  
2 S.-Q. Zhang, *Ionics*, 2021, **27**, 339–349. View Article Online  
DOI: 10.1039/D0MA00227G
- 3 51. J. Zhang, G. Li, J. Liu, Y. Liu, R. Yang, L. Li, Q. Zhao, J. Gao, G. Zhu and B. Zhu,  
4 *Sensors and Actuators B: Chemical*, 2023, **378**, 133108.
- 5 52. D. Manno, L. Torrisi, L. Silipigni, A. Buccolieri, M. Cutroneo, A. Torrisi, L. Calcagnile  
6 and A. Serra, *Applied Surface Science*, 2022, **586**, 152789.
- 7 53. S. Ramaraj, M. Sakthivel, S.-M. Chen and K.-C. Ho, *Analytical chemistry*, 2019, **91**,  
8 8358–8365.
- 9 54. S. Gadipelli, J. Guo, Z. Li, C. A. Howard, Y. Liang, H. Zhang, P. R. Shearing and D. J.  
10 Brett, *Small Methods*, 2023, **7**, 2201557.
- 11 55. S. Rajkumar, S. Gowri, S. Dhineshkumar, J. P. Merlin and A. Sathiyam, *New Journal*  
12 *of Chemistry*, 2021, **45**, 20612–20623.
- 13 56. U. S. Veerasamy, S. Palani, Y. Fujita, Y. Matsunaga, T. Kuzuya, C. Sekine and Y.  
14 Mona, *Advanced Sensor and Energy Materials*, 2025, 100169.
- 15 57. R. Iimura, T. Hasegawa and S. Yin, *Inorganic Chemistry*, 2022, **61**, 2509–2516.
- 16 58. P. Dubey, V. Shrivastav, M. Jain, K. K. Pant, P. H. Maheshwari and S. Sundriyal,  
17 *Energy & Fuels*, 2023, **37**, 8659–8671.
- 18 59. S. M. Abdullah, M. A. Marwat, K. M. Adam, Z. U. Din, M. Humayun, M. R. A. Karim,  
19 E. Ghazanfar, M. Bououdina, U. Hamayun and M. S. Youssef, *RSC advances*, 2024,  
20 **14**, 14438–14451.
- 21 60. X. He, Y. Zhao, R. Chen, H. Zhang, J. Liu, Q. Liu, D. Song, R. Li and J. Wang, *ACS*  
22 *Sustainable Chemistry & Engineering*, 2018, **6**, 14945–14954.
- 23 61. S. Gopi and S.-F. Wang, *ACS Applied Nano Materials*, 2025, **8**, 924–934.
- 24 62. M. Govindaraj, M. K. Muthukumar, P.-C. Tsai, K. Prakasham, G. Andaluri, M.  
25 Eswaran, V. K. Ponnusamy and J. Arockia Selvi, *Food Chemistry*, 2025, **495**, 146387.
- 26 63. S. Srivastav, S. Singh and S. K. Meher, *Langmuir*, 2023, **40**, 362–379.
- 27 64. E. Elanthamilan, S. Rajkumar, R. Rajavalli and J. P. Merlin, *New Journal of Chemistry*,  
28 2018, **42**, 10300–10308.
- 29 65. Z. Yan, S. Luo, Q. Li, Z. S. Wu and S. Liu, *Advanced Science*, 2024, **11**, 2302172.
- 30 66. F. Zhang, T. Zhang, X. Yang, L. Zhang, K. Leng, Y. Huang and Y. Chen, *Energy &*  
31 *Environmental Science*, 2013, **6**, 1623–1632.
- 32



1  
2  
3  
4

Open Access Article. Published on 28 April 2026. Downloaded on 4/29/2026 12:56:15 AM.  
This article is licensed under a Creative Commons Attribution 3.0 Unported Licence.



## Data availability

View Article Online  
DOI: 10.1039/D6MA00227G

Data related to the manuscript content will be made available upon request.

